X-283-67-493

NASA TM X-55952

X-RAY OPTICS
PART I

J. MANGUS

SEPTEMBER 1967

NASA

GODDARD SPACE FLIGHT CENTER

GREENBELT, MARYLAND

X-283-67-493

X-RAY OPTICS

PART I

J. Mangus

September 1967

GODDARD SPACE FLIGHT CENTER
Greenbelt, Maryland

X-RAY OPTICS

PART I

J. Mangus

September 1967

GODDARD SPACE FLIGHT CENTER
Greenbelt, Maryland

X-RAY OPTICS

PART I

J. Mangus

SUMMARY

This series of reports relates the status of research on the fabrication of glancing incidence optical components at the Goddard Space Flight Center. This work has been performed by the Optics Branch of the Experimental Fabrication and Engineering Division under SRT Program 283-188-38-01-10.

The investigation has four aspects — theory, design, fabrication and testing. This report is primarily concerned with the elementary theory and design of a two element glancing incidence telescope. The GSFC X-ray Telescope Experiment for ATM, a Type 1 telescope (concave parabola followed by a concave hyperbola), is analyzed using a modified ray tracing program outlined by Wolter[1]. It is shown that the image quality of such a system can be significantly improved by matching the detector to the optimum focal surface and by vignetting rays which contribute to the flare in comatic images. Vignetting is accomplished by reducing the hyperbola element to approximately one half of its length from an unvignetted configuration. The total weight of the hyperbola element is, therefore, reduced by one half, resulting in a savings of material cost and fabrication time. The imaging properties of a one-third scale ATM type telescope are discussed.

X-RAY OPTICS

PART I

INTRODUCTION

The desire of scientist to extend observations of primarily solar phenomena into the spectral region below 500 Å has spurred the investigation of using glancing incidence type optics to obtain spatial as well as spectral information[2,3] The gathering of spatial information in the X-ray region is not new as some investigators have used an array of devices ranging from pinhole cameras to various mirror arrangements[4-7]. However, surfaces of rotation appear to have unique characteristics worth investigation. These are the component rigidity and relatively large photon gathering capacity combined with the ability to provide spatial information.

An excellent paper by Wolter [1,4] describes in detail some of the fundamental properties of systems which are under investigation at GSFC. Wolter, however, approached the problem from the aspect of applying these optical systems to X-ray microscopy. Furthermore, it has been evident that a more detailed account of the imaging properties is necessary to acquaint the scientist with the theoretical limitations of such systems and also to reveal to the optical technician what one may expect to see when fabricating non-normal incidence components and systems.

It is important to note that the term "non-normal incidence" is taken to be synonomous with "glancing incidence" for it is precisely from this non-normal incidence characteristic that imaging problems arise.

The principal reason for using non-normal incidence configuration is to realize the efficient reflection of energy in the X-ray region. Figure 2 illustrates this fact quite clearly, for as the angle of incidence proceeds from normal incidence to near normal incidence and finally to non-normal incidence the amount of energy reflected increases.

A parabola of revolution might appear as the first likely candidate for use as a glancing incidence element. However, objects imaged off axis by this contour suffer severe aberrations. It has been demonstrated that the reason for this effect is that imaging characteristics of single glancing incidence elements grossly violate the Abbe Sine Condition [1]. This may be understood if one considers that a perfect image of a point source is formed at the center of curvature of a collapsing spherical wavefront. Therefore, it is the function of the optical component to convert the wavefront emanating from the object point into a

spherical wavefront which will collapse onto the corresponding image point. The Sine Condition is written in the form[8]

$$\frac{h}{\sin \theta} = \text{constant} = r \tag{1}$$

for a point source at infinity, where h is the radial height from the optical axis at which the incident ray strikes the aperture and θ is the angle the reflected ray makes with the optical axis. Any deviation from the principal spherical surface defined by Equation (1) may then be thought of as contributing to imperfections in the image. Clearly, a single glancing incidence element does not conform to the Sine Condition.

However, for a combination of glancing elements such as the concave parabola-concave hyperbola (labeled type 1 by Wolter) illustrated in Figure 2, the noncompliance of the principal surface with Equation (1) or more precisely the offense against the Sine Condition is given by[1]

$$OSC = \Delta r = r \Delta \alpha_2 \tan \frac{\alpha_2}{2} \tag{2}$$

The above combination may then be designed to minimize OSC and also serve as an efficient X-ray collector. If the effective aperture is given by A, then

$$A \approx 2\pi y_{p\,min}\, r \Delta \alpha_2$$

where

$$s = r \Delta \alpha_2$$

Furthermore $\alpha_2 = 4\theta_{max}$ where the maximum slope angle θ_{max} is small (i.e., $\theta_{max} \sim 1°$) then

$$\Delta r \propto \frac{A \theta_{max}}{y_{p\,min}}$$

Hence, to minimize OSC for a given minimal collecting area A, and maximum glancing angle θ max, (equal to the maximum slope angle of the parabola for an on axis ray) the diameter of the aperture must be increased.

Designs for type 1 telescopes are rather inflexible as all of the definitive parameters are fixed if the maximum slope angle, minimal collection area and focal length $f = r$, are specified. From Appendix I and Figure 2

$$y_{p\,min} = f \sin 4\theta_{max} = y_{h\,min} \tag{3}$$

$$p = y_{p\,min} \tan \theta_{max} \tag{4}$$

$$c = f/2 \tag{5}$$

$$a = f\,(2 \cos 2\theta_{max} - 1)/2 \tag{6}$$

$$b = (c^2 - a^2)^{1/2} \tag{7}$$

$$y_{p\,max} = \left[\frac{A}{\pi} + y_{p\,min}^2\right]^{1/2} \tag{8}$$

The radial image size, τ, in the Gaussian focal plane can be calculated for a half field angle δ from the equation

$$\tau = f \sin \delta \frac{1 - \cos 4\theta_{max}}{2 \cos 4\theta_{max}}$$

However, the above formula only applies with accuracy for imaging by the zone of intersection of the parabola and hyperbola. It is therefore necessary to develop a ray tracing procedure for a more comprehensive assessment of the imaging properties of the telescope.

RAY TRACING PROCEDURE

A set of 19 rays are traced from points on a circle defined by the intersection of the YZ plane with the parabolic aperture. Rays are traced from points on this circle spaced at ten degree circumferential increments of an angle ϕ about the optical axis, starting with the positive y axis ($\phi = 0°$) through $\phi = 180°$ to the negative y axis. It is necessary to only trace rays through one half the aperture because of the symmetry of the telescope. A total of eleven sets

(denoted as S1, S2, ... S11,) or 209 rays are traced for each half field angle, δ. The X intercept of each set of rays is such that ten percent of the full aperture area is encompassed in the zone defined by two successive sets of rays. The locations of the YZ ray intercept or focal plane is moved in and out of the Gaussian focus (M = 0). Positive values of M indicate that the focal plane is moved toward the telescope whereas negative values of M indicate that the focal plane is moved away from the telescope. Half field angles were varied from δ = .000 to δ = .006 radians in .001 radian increments.

Details of the ray trace procedure which closely follow that outlined by Wolter, are outlined in the Appendix II. A 7094 computer was used to perform the computations.

TELESCOPE DESIGN

The first telescope design to be traced using the program described above is that of a type 1 (concave parabola followed by a concave hyperbola) configuration. Using the formulation of Equations 3, 4, 5, 6, 7 the configuration of the telescope is given by the following parameters if f = 75 inch, θ max = 0.916 degrees and A = 2.3 in^2

p = 0.07663156 inch

a = 37.4616644 inch

b = 1.6951988 inch

c = 37.500000 inch

$y_{p\,min}$ = 4.792896 inch

$y_{p\,max}$ = 4.868791 inch

This design was used as the basic configuration for the GSFC ATM X-ray telescope experiment.

IMAGING PROPERTIES

The spot diagrams in Figure 3A depict the image of a star formed by the telescope in the Gaussian focal plane for various half field angles. The image becomes severely elongated in the XY or tangential plane as greater field angles are viewed. As the focal plane is moved toward the telescope, M > 0, the image size for large values of δ decrease in size, however, for large displacements of the focal plane (M > .020) there is corresponding increase in the images made at small field angles, Figure 3B.

The magnitude of this effect on the tangential spot diameter versus focal plane location is shown in Figure 4. As is evident in the diagram, there is a leveling off or a best focus region for each half field angle. This arises from the fact that the telescope suffers from curvature of field, i.e., the tangential rays incident on the front and rear aperture of the parabola are not imaged in the same plane. The longitudinal and laterial displacement of these rays results in an image which appears to be sheared as illustrated by the half aperture spot diagram in Figure 5. It is evident that although the image can be decreased in size by displacement of the focal plane toward the telescope that the downward or comatic flare of the image is still present to some degree.

One may use a vignetting technique to minimize the flare effect, first by locating where the tangential rays are incident on the hyperbolic surface, Figure 6, correlating this information with their relative displacement in the XY plane, and then reducing the length of the hyperbola such that the unwanted rays are vignetted. The procedure for using this technique is as follows: The hyperbola X intercepts are plotted versus circumferential angle ϕ for each half field angle δ and every set of rays. There is but one X intercept on the hyperbola for each of the 11 sets of rays for $\delta = 0$. For half field angles greater than $\delta = 0$, the X intercepts vary along the length of the hyperbola within a given set and have common cross over positions approximately located at $\phi = 90°$ and $\phi = 270°$. It is seen that for field angles greater than $\delta = 0$, using the $\delta = 0$, X intercept as a reference that the X intercept within a given set of rays is closer to the front of the telescope for circumferential angles where $90° \leq \phi \leq 270°$ and correspondingly the X intercept moves away from the front of the telescope and thereby elongates the hyperbola for $0° \leq \phi < 90°$ and $270° < \phi \leq 360°$.

As stated previously, the tangential rays from the upper and lower rim of the parabola do not have a common focus. It is seen from Figure 7 that the meridonal tangential rays, $y_{p\,max}$, focus is closer to the telescope than that of the lower tangential rim rays, $y_{p\,min}$. There are therefore two cross over locations of these rays between the two tangential foci. (It is in between these cross over points where the leveling off or minimization in image size occurs as was noted in Figure 4.) The ray contributing to the downward most portion of the image comatic flare in the YZ plane of the crossover point closest to the Gaussian focal plane arises from the front zone of the parabola, $y_{p\,max}$, at $\phi = 0°$. The cross over point is approached as $\phi \rightarrow 180°$. It is therefore evident that those rays incident on the meridonal zone on the parabola in the vicinity of $\phi = 0°$ are the source of the comatic flare. However, it is precisely these rays which are also incident on the last portion of the hyperbola. Hence, if a back portion of the hyperbolic element is eliminated, these rays will be vignetted and the comatic flare suppressed to some degree depending on just

how short the hyperbola is made. In order to minimize the vertical diameter of the image, the length of the hyperbola was selected such that the last ray incident on the lower rim of the hyperbola for $\phi = 0°$, intersects the ray originating from $\phi = 180°$ at $y_{p\,min}$ in the same YZ plane which contains the cross over point closest to the Gaussian focal plane. This is shown in Figure 7 for $\delta = .004$ radian. For the design under investigation, this technique results in halving the length of the hyperbola.

The loss of energy in the image (assuming a one-to-one correspondence to the decrease in effective aperture) is plotted in Figure 8 versus the length of the hyperbola. Vignetting at large field angles is substantial, but a considerable reduction of image size is realized. A comparison of unvignetted and vignetted images, Figure 9, for each field angle illustrates the image compacting quite vividly. The angular subtense of the tangential diameter of these images in their optimum focal positions is indicated in Figure 10.

The shape of the optimum focal plane can be approximated as a hyperbola described by the equation

$$\frac{(x + a)^2}{a^2} - \frac{y^2}{b^2} = 1$$

where

$a = .08476$ inch

$b = .30151$ inch

However, it is not always possible to shape the image detector to the optimum focal surface. It is therefore informative to examine the distribution of energy within an image in a flat focal surface as well as the optimal focal shape. As stated previously, eleven zones of the parabola were traced, each pair of zones encompassing 10% of the field aperture area. The distribution of energy within an image may then be correlated to the area circumscribed by these sets of rays. This energy (area) distribution was measured by incrementally summing the distribution of the area for each zone in the $\pm$ Z direction within the YZ focal plane. There is an obvious increase in energy at the image core, Figure 11, as one progresses from the Gaussian to optimal focus. (The arrows on the Y axis indicate the point at which vignetting takes place if the hyperbola is reduced to one half of its length from the unvignetted configuration.)

Resolving Power

To what degree this telescope will resolve two closely space point sources is difficult to predict. It is clear that by using selective vignetting and shaping the detector to the contour of the optimum focal surface that the relative percent of the light in the hard core of the image is increased. This judgment has been made strictly on the basis of geometrical ray tracing. However, there are other factors which must be considered when predicting image quality.

First, one must realize that in practice, the resolving power will also be dependent upon the optical quality of the contour used for imaging. Geometrical optics can validly be applied to a surface where the wavelength is small compared to the dimensions of the surface roughness. In this case, the reflectance in a given direction would only be a function of the slope of the surface imperfection. As the wavelength becomes longer diffraction and scattering become important factors and the reflectance is determined by the size and spatial frequency as well as the slope of the imperfections. Finally, as the wavelength becomes large compared to the dimensions of the surface roughness, diffraction phenomena dominates the reflectance characteristics of the surface. Unfortunately, the above considerations are further complicated when perfect conductors are not used as the reflecting element and one must therefore be concerned about polarization as well as phase and amplitude effects.

To further illustrate the magnitude of the problem for predicting the image quality of an x-ray telescope, consider the data in Table I as applied to the telescope designed to form images in the spectral region 6Å to 26Å. From Table I it is clear that the roughness of optically polished surfaces span the spectral region of interest. Variations in the measurements of the root mean square roughness, σ, of a given material are attributed to melt differences and the techniques applied to polish and measure the surface roughness. Because it is desired to make a surface as smooth as possible it is preferable to use and polish a material such as fused silica or Cer-Vit using the bowl feed technique. Semi-conductors, conductors, and conductive coatings have not been considered here because of the lack of quantitative data. But, even for the super smooth surfaces of fused silica or Cer-Vit, the wavelength is not large compared to the surface roughness. It is therefore to be expected that diffraction and scattering effects will be convolved with the geometrical imaging characteristics of soft x-ray telescopes.

The maximum permissible surface roughness height may be calculated from a strictly geometric viewpoint as illustrated in Figure 12. The optical path difference, δ, between rays A and B is calculated to be given by:

Table I

Roughness of Optically Polished Surfaces

Material	σ_{rms} [9-14]
Flint glass	154Å[a], 41Å[f]
Plate glass	68Å[a], 25Å[d], 40Å[e], 18Å[f]
Glass Slide	56Å[b]
Pyrex	51Å[a], 14Å[f]
Fused silica	36Å[a], 3Å[d], 9.6Å[f], 2.7Å[d], 7Å[d] <
Borosilicate crown glass	10Å[c]
Cer-Vit	6.6Å[d], 6.9Å[d], 10.1Å[d], 7Å[d] <

[a] Fresh feed polishing technique

[b] Fire polished

[c] Not stated (Ref. 11)

[d] Bowl feed polishing technique

[e] Not stated (Ref. 10)

[f] Not stated (Ref.9)

$$\delta = h\left(\frac{1 - \cos 2\theta}{\sin \theta}\right)$$

where θ is the glancing angle. One finds by applying the Rayleigh limit to the optical path difference that

$$h = \frac{\lambda}{4}\left(\frac{\sin \theta}{1 - \cos 2\theta}\right) \tag{9}$$

Therefore, at a glancing angle of $\theta = 1°$, $h/\lambda \approx 7.1$ which, for $\lambda = 25\text{Å}$, corresponds to approximately one-thirtieth of a wavelength in the visible. This analysis, however, treats only the phase relationship of the focused beam.

The effects of surface roughness on the amplitude of the reflected beam are quite complicated. The most thorough research in the literature[9,15] has been for cases of normal incidence and $\lambda/\sigma << 1$.

A mathematical treatment of the subject by Porteus[16] has given some insight as to the complexity of the problem. The reflected beam is considered to be divided into two parts, namely, that which is coherently reflected and that which is incoherently reflected. The light which is incoherently reflected gives rise to wave fronts which are uncorrelated in phase unless they originate from a localized region on the surface, whereas the coherently reflected light consists of mutually interfering wave fronts from all parts of the reflecting surface. The coherently reflected component, R_c, is related to the limiting reflectance R_o (i.e., as $\sigma \to 0$) by the expression

$$\frac{R_c}{R_o} = \cos^2 \psi \left| \int_{-\infty}^{+\infty} D(z)\, e^{\left[-4\pi i (z/\lambda) \cos \psi\right]} dz \right|^2 \tag{10}$$

where ψ is the angle of incidence, z is the height of the surface irregularity and $D(z)$ is the marginal density function of the surfaces heights which is related to the total surface joint density function $D_j(\bar{s}, z, z')$ by

$$D(z) = \int_{-\infty}^{+\infty} D_j(\bar{s}, z, z')\, dz'$$

Although the surface heights z and z' are statistical variables at the points $\bar{r}$ and $\bar{r}'$, respectively, they are not mutually independent because of the continuity of the surface and therefore maintain a correlation which depends on $\bar{r} - \bar{r}'$ represented as $\bar{s}$.

The incoherent term for the reflectance, R_i, from a uniformly rough isotropic surface is given by

$$\frac{R_i}{R_o} = \frac{1}{\lambda_2}\int\int\int\int\left[D_j\,(s,\ z,\ z') - D(z)\,D(z')\right] e^{\left[\frac{-4\pi i}{\lambda}(z-z') - i\bar{k}_d \cdot \bar{s}\right]} dz\,dz'\,d\bar{s}\,d\Omega \tag{11}$$

where $\bar{k}_d$ represents the propagation vector of the diffracted wave fronts. Porteus has shown that although Equations (10) and (11) may be used to describe the reflectance characteristics of rough surfaces at normal incidence where $\lambda >> \sigma$, there still exists a great deal of uncertainty when trying to predict short wavelength behavior of the incoherent reflectance (i.e., as $\lambda \to \sigma$). The reason for this difficulty arises from the fact that it is demonstrated that obvious parameters such as the root mean square roughness σ, the surface slope m and the autocovariance length a do not necessarily govern incoherence reflectance in this range because of their common derivation from the autocovariance function

$$< z\,z' > - < z > < z' >$$

It is further demonstrated that subtle differences in the choice of a joint density function markedly influence the short wave length behavior. The reason that the above complexities have been emphasized is as follows.

Consider an isotropic surface consisting of facets of random size and shape which are aligned parallel to a reference plane but at random levels relative to this plane. Further choose that the probability, $p(s)$, that two points chosen at random on the surface a distance apart will lie at an equal level relative to the reference plane. If then $p(s)$ and $D(z)$ are required to be Gaussian the coherent reflectance for normal incidence is given as

$$R_c = R_o \exp\left[-(4\pi\sigma/\lambda)^2\right]$$

while the incoherent reflectance is

$$R_i = R_o \left\{1 - \exp\left[-(4\pi\sigma/\lambda)^2\right]\right\} \left\{1 - \exp\left[-(\pi a\alpha/\lambda)^2\right]\right\}$$

where α is the semi vertex angle of the cone of acceptance. These last two equations describe very well the behavior of light reflected at normal incidence where $\sigma/\lambda << 1$.

If $\sigma \cos \psi$ is substituted for σ to account for the angle of incidence then

$$R_c = R_o \exp\left[- (4\pi\sigma \cos \psi/\lambda)^2\right] \tag{12}$$

From the previous consideration of applying the Rayleigh limit it was shown for $\psi = 90° - \theta = 89°$ at $\theta = 1°$ that $\sigma/\lambda \approx 7.1$. However, applying these values to Equation (12) it is found that

$$\frac{R_c}{R_o} \approx 9.5\%$$

Clearly a surface which closely approximates the joint density function described above and a roughness on the order of 7λ is unsatisfactory. If the surface roughness is on the order of magnitude of the wavelength, $\sigma \approx \lambda$, such as could be the case at $\lambda = 6$Å for a bowl feed polished fused silica surface then,

$$\frac{R_c}{R_o} \approx 95\%$$

This reflectance is far more acceptable than the previous example; however, it implies that the parabola and hyperbola contours can be polished to an accuracy of $\lambda/500$ in the visible region. It is more probable that one would achieve a surface which has a super smooth surface with a contour which only approximates the aspheric contour. Then one has two surface roughness parameters, σ_1 and σ_2, which describe respectively the super smooth surface and the "waviness" or larger variations from the prescribed contour. This latter condition is given as

$$\frac{R_c}{R_o} = \exp\left[- (4\pi/\lambda)^2 \left(\sigma_1^2 + \sigma_2^2\right) \cos^2 \psi\right]$$

and

$$\frac{R_i}{R_o} = \left\{ \exp\left[-\left(\frac{4\pi\sigma_1 \cos\psi}{\lambda} \right)^2 \right] - \exp\left[-\left(\frac{4\pi}{\lambda} \right)^2 \left(\sigma_1^2 + \sigma_2^2 \right) \cos^2\psi \right] \right\}$$

$$\times \left\{ 1 - \exp\left[-\left(\frac{\pi a_2 \alpha}{\lambda} \right)^2 \right] \right\} + \left\{ 1 - \exp\left[-\left(\frac{4\pi\sigma_1}{\lambda} \cos\phi \right)^2 \right] \right\}$$

$$\times \left\{ 1 - \exp\left[-\left(\frac{\pi a_1 \alpha}{\lambda} \right)^2 \right] \right\}$$

if one again assumes that σ can be replaced by $\sigma \cos\psi$. It is apparent that in order to achieve a reasonable coherent reflectance that $\sigma_2 \rightarrow \sigma_1$. However, again it is emphasized that the above treatment and experimental verifications have been for the case of normal incidence. There is a definite need for a precise study of glancing incidence conditions.

Secondly, the annular aperture characteristic of x-ray optics in theory should contribute to diffraction phenomena which would increase the theoretical resolving power of a diffraction limited system by narrowing the half intensity width of the principal maxima. However, the preceding ray trace results indicate that the system would only be diffraction limited over a field encompassing a few seconds of arc. Indeed, the on-axis performance is the only probable area where one would expect to see diffraction limited performance. A drawback of the annular aperture is that the redistribution of energy is such that the relative intensity of the secondary diffraction rings is increased when compared to the principal maximum as shown in Figure 13. The result is that although the Rayleigh criterion can be exceeded, the background is also increased and a loss in contrast is to be expected.

In summary, it should be noted that incoherent scattering, diffraction, and the geometrical imaging properties of the Type I soft x-ray telescope all tend to decrease the image contrast.

Experimental Results

Some interesting effects have been observed in the imaging properties of an x-ray telescope fabricated in this laboratory. The telescope, which was fabricated from borosilicate crown glass, is approximately one-third the scale of the GSFC ATM system described above. The ratio of the radii which define the annular aperture is defined as

$$\epsilon \equiv \frac{y_{p\,min}}{y_{p\,max}} = 0.984$$

where $2\,y_{p\,max} = 82.6262$ mm. The focal length, f, of the telescope was measured to be 627.761 mm.

The photographs in Figures 14A and 14B illustrate the telescope image quality when viewing a 0.58 arc second source in green light ($\lambda = .5461\mu$). If the concentric rings for the on-axis image arise from a diffraction limited quality, then the radial intensity distribution in the image must comply with the equation describing the diffraction by an annular aperture. This equation is [17]

$$\frac{I(p)}{I_o} = \frac{1}{(1-\epsilon^2)^2}\left[\frac{2J_1(x)}{x} - \epsilon^2\, 2\frac{J_1(\epsilon x)}{\epsilon x}\right]^2 \qquad (13)$$

where

$$x = \frac{2\pi}{\lambda}\, y_{p\,max}\, \phi$$

ϕ = angular ring radius at a point, P

$I(p)$ = intensity at point, P

I_o = incident intensity

$J_1(x)$ & $J_1(\epsilon x)$ = Bessel functions of the first order

The intensity minima are determined by setting the above equation to zero and solving the resulting equation

$$J_1(x) = \epsilon\, J_1(\epsilon x) \qquad (14)$$

Table II is a listing of x for minimas when $\epsilon = 0.984$.

If the radii of the diffraction minimas as measured off the photographs are designated as r_i, where i is the minima number counting from the center of the diffraction pattern, and M is denoted as the magnification incurred in the photographic process, then

$$r_i = f\,\phi_i\,M$$

Table II

Listing of x For Minimas When $\epsilon = 0.984$.

Minima #	x
1	2.436
2	5.566
3	8.722
4	11.889
5	15.052
6	18.216

However,

$$\phi_i = \frac{x_i \lambda}{2 \pi y_{p\,max}}$$

Therefore,

$$x_i = \frac{2 \pi y_{p\,max}}{f \lambda M} r_i = k r_i \qquad (15)$$

The quantity x_i was calculated from Equation (15) using the system parameters outlined above and the measurements of r_i when $M = 43$. The results are listed in Table III for $k = 176.089\ cm^{-1}$.

It is clear from Table III that the on-axis performance of the telescope is diffraction limited. The discrepancies in the larger values of x_i are in part due to the slightly oval shape of the ring pattern, which indicates that there is a defect in the pinhole used as a source and/or in the circular symmetry of the telescope optics.

Table III

Minima #	Minima Radii	Experimental	Theoretical	Error
i	r_i	x_i	x	%
1	.013000 cm	2.289	2.436	−6.0
2	.033225 cm	5.851	5.566	+5.1
3	.051350 cm	9.042	8.722	+3.7
4	.071100 cm	12.520	11.889	+5.3
5	.090375 cm	15.914	15.052	+5.7
6	.108140 cm	19.042	18.216	+4.5

At 0.5° off axis the diffraction rings are still present; however, some flare in the image is evident as well as scattering. Figures 15A and 15B illustrate the loss in sharpness of the image on axis as the angular subtense of the object is increased to 2.32 and 5.79 arc seconds, respectively.

REFERENCES

1. Wolter, H., (1952) Annalin der Physik, Series 6, 10, 94.

2. Baez, A. V., (1960) J. Geophys. Res., 65, 3019.

3. Giaconni, R. and Rossi, B., (1960) J. Geophys. Res., 65, 773.

4. Wolter, H., (1952) Annalin der Physik, Series 6, 10, 286.

5. Kirkpatrick, P., (1950) Nature, 166, 251.

6. Montel, M., (1954) Comptes Rendus, 239, 39.

7. Kirkpatrick, P. and Baez, A. V., (1948) J.O.S.A. 38, 766.

8. Born, M. and Wolf, E., (1959) Principles of Optics, Section 4.5.1, Permagon Press.

9. Bennett, H. E. and Porteus, J. O., (1961) J.O.S.A., 51, 123.

10. Heavens, O. S., (1951) Proc. Phys. Soc., London, 3, 64, 419.

11. Holland, L., (1964) The Properties of Glass Surfaces, John Wiley & Sons, Inc.

12. Koehler, W. F. and White, W. C., (1955) J.O.S.A., 45, 1011.

13. Koehler, W. F., (1953) J.O.S.A., 43, 743.

14. Dietz, R. W. and Bennett, J. M., Applied Optics (1967) 6, 1275.

15. Bennett, H. E., (1963) J.O.S.A., 53, 1389.

16. Porteus, J. O., (1963) J.O.S.A., 53, 1394.

17. Born, M. and Wolf, E., (1959) Principles of Optics, Section 8.6.2, Permagon Press.

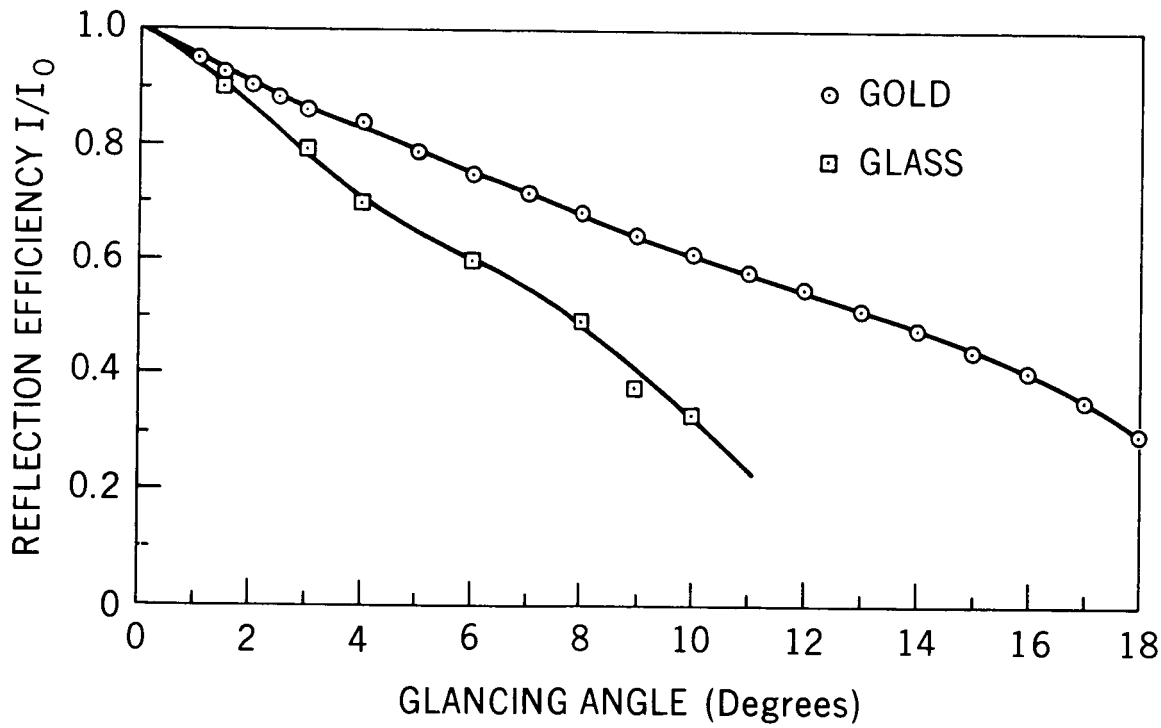

Figure 1. Reflection Efficiency of Gold and Glass Surfaces Versus Glancing Angle

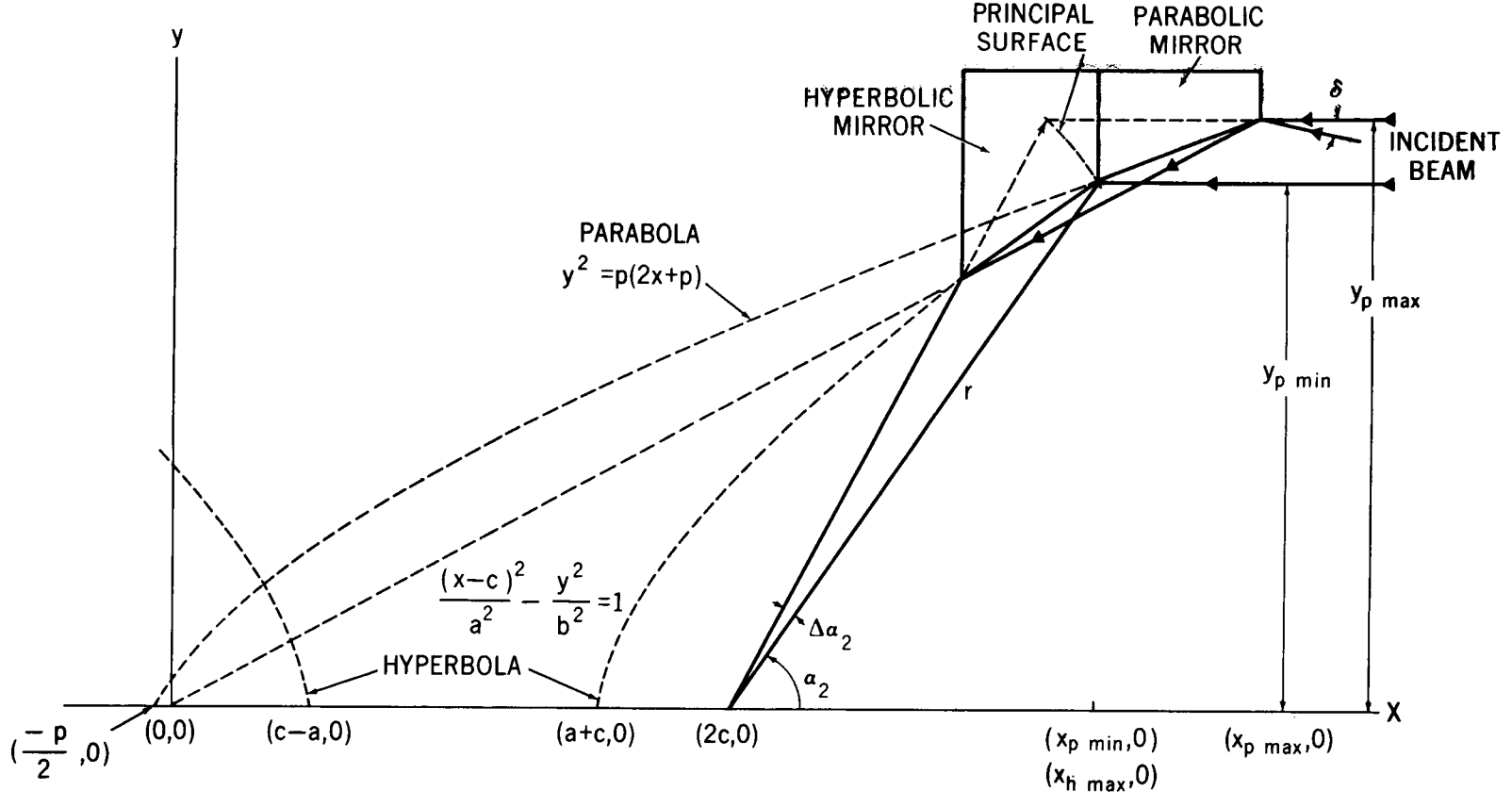

Figure 2. Type 1 X-Ray Telescope Geometry

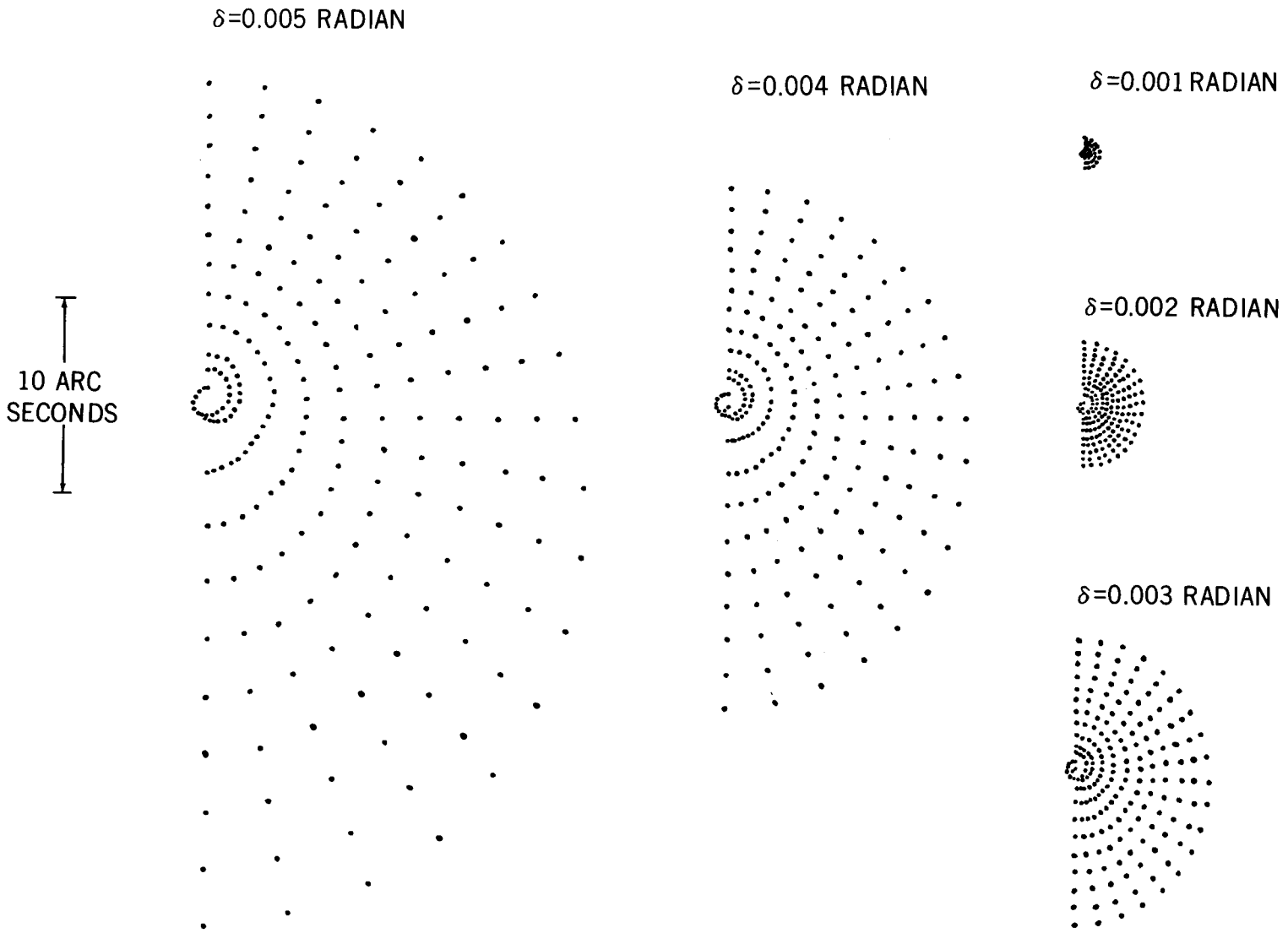

Figure 3A. Spot Diagrams at Gaussian Focus, M = 0.00 inch

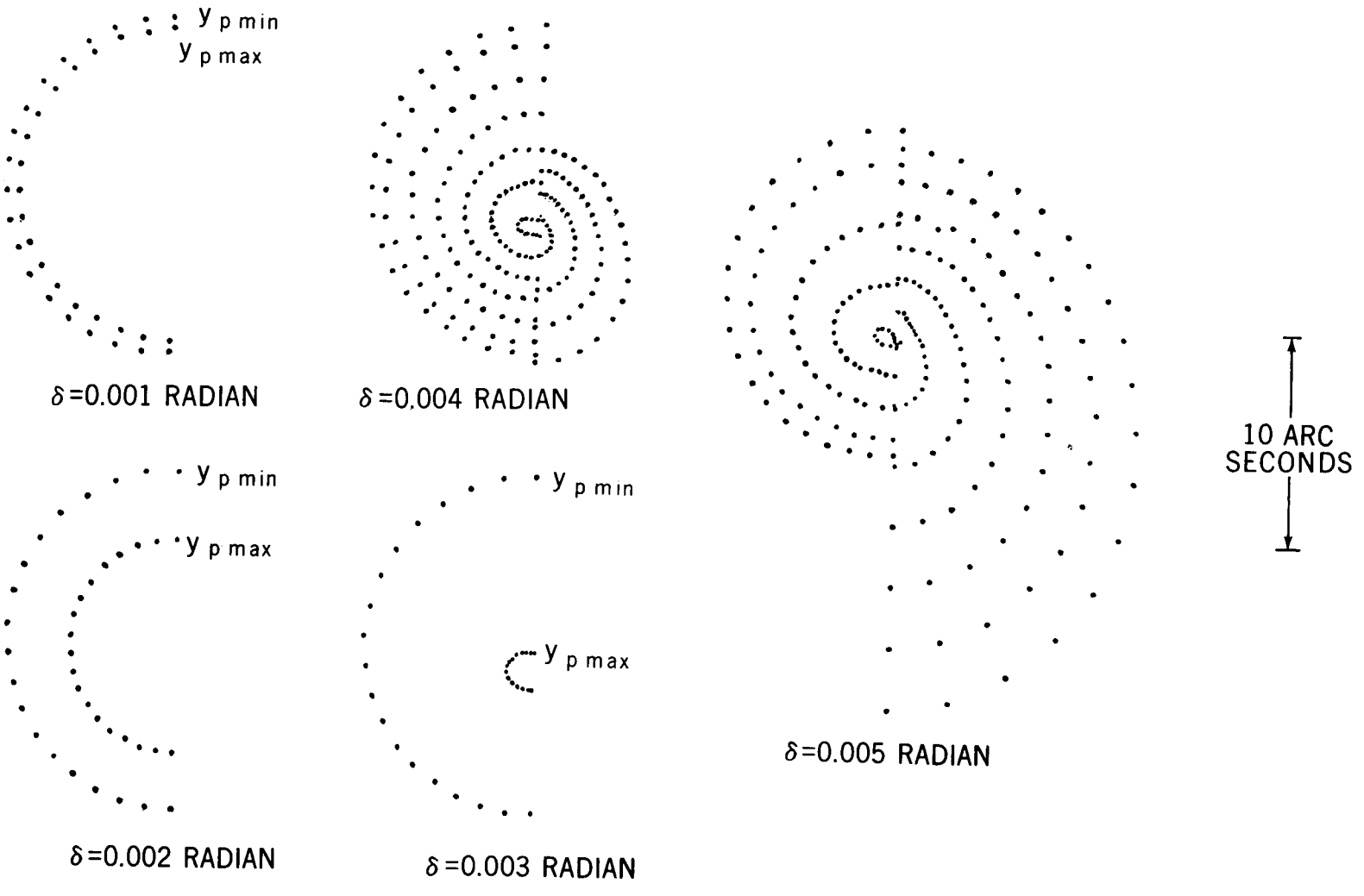

Figure 3B. Spot Diagrams Inside Gaussian Focus, M = +0.05 inch

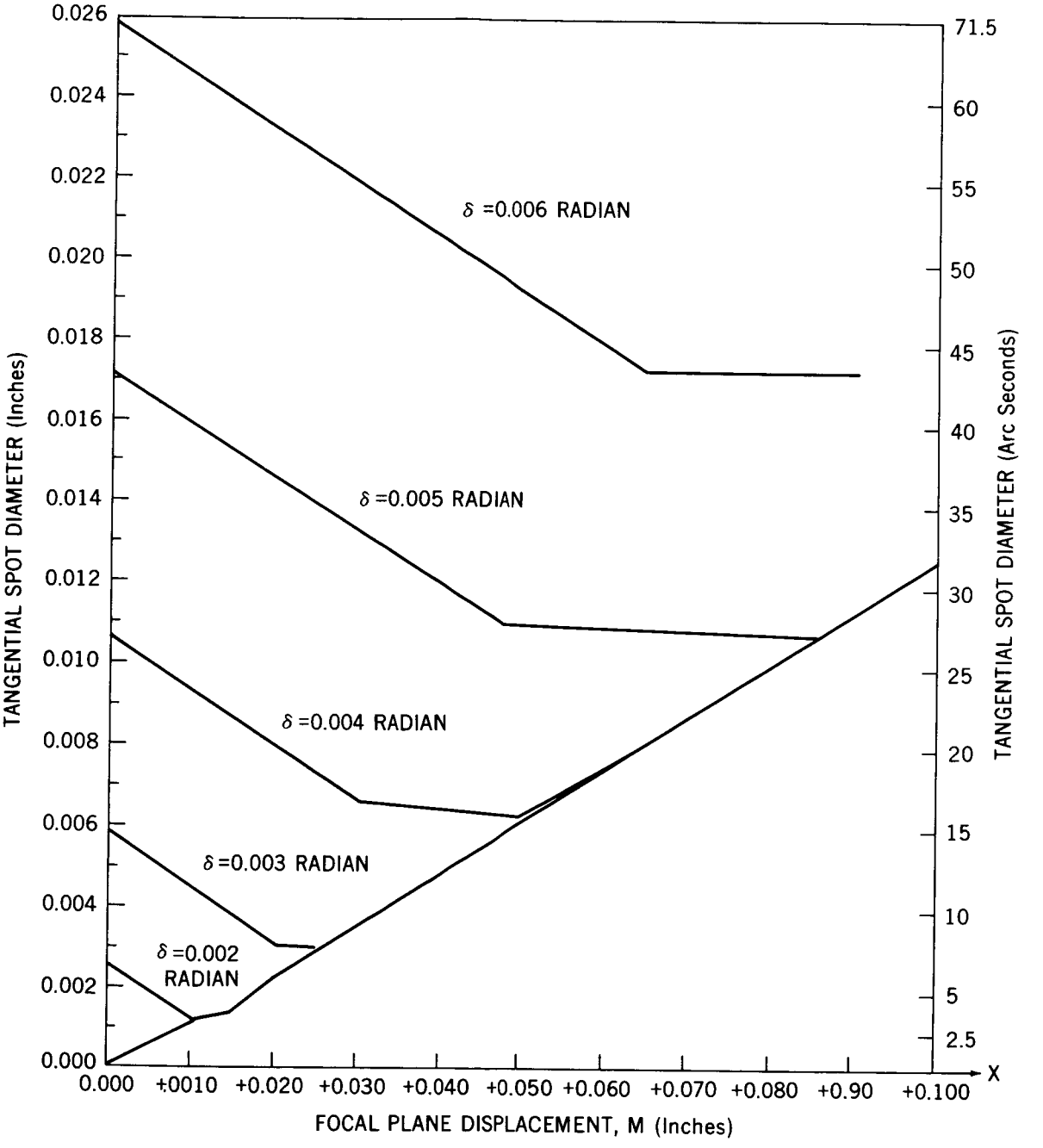

Figure 4. Tangential Spot Diameter Versus Focal Plane Location

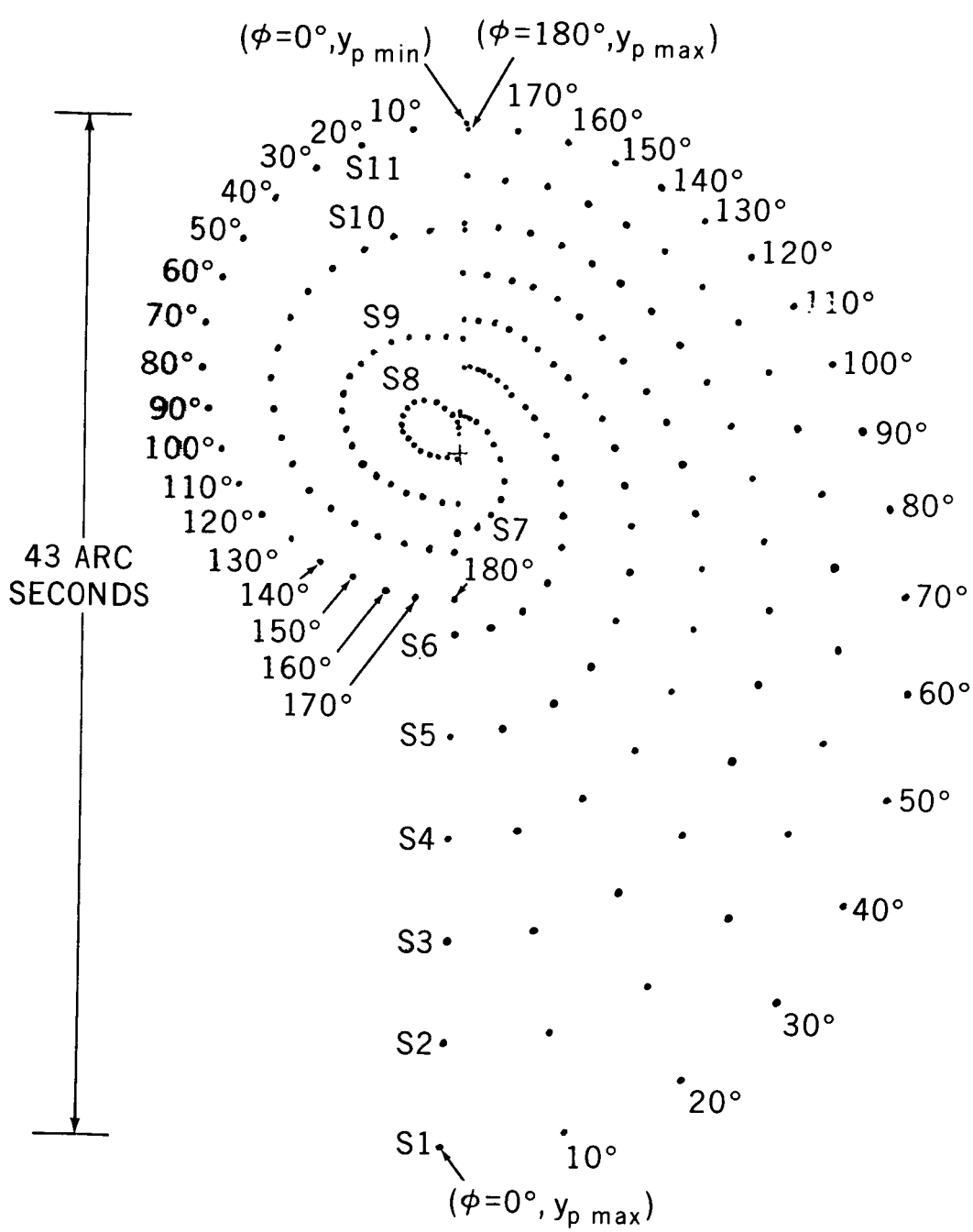

Figure 5. Half Aperture Spot Diagram

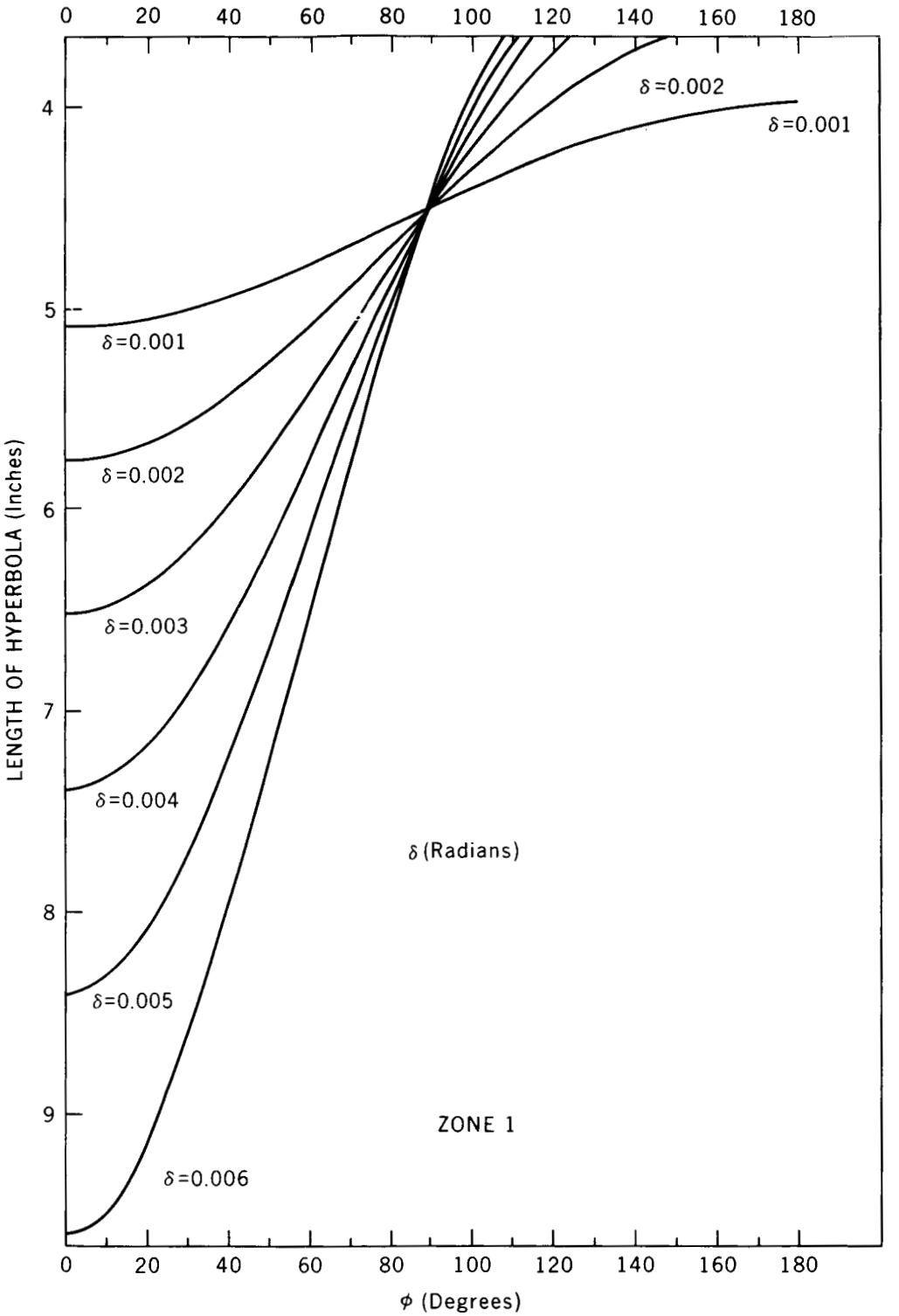

Figure 6A. Hyperbolic Intercept Versus Aperture Circumferential Angle

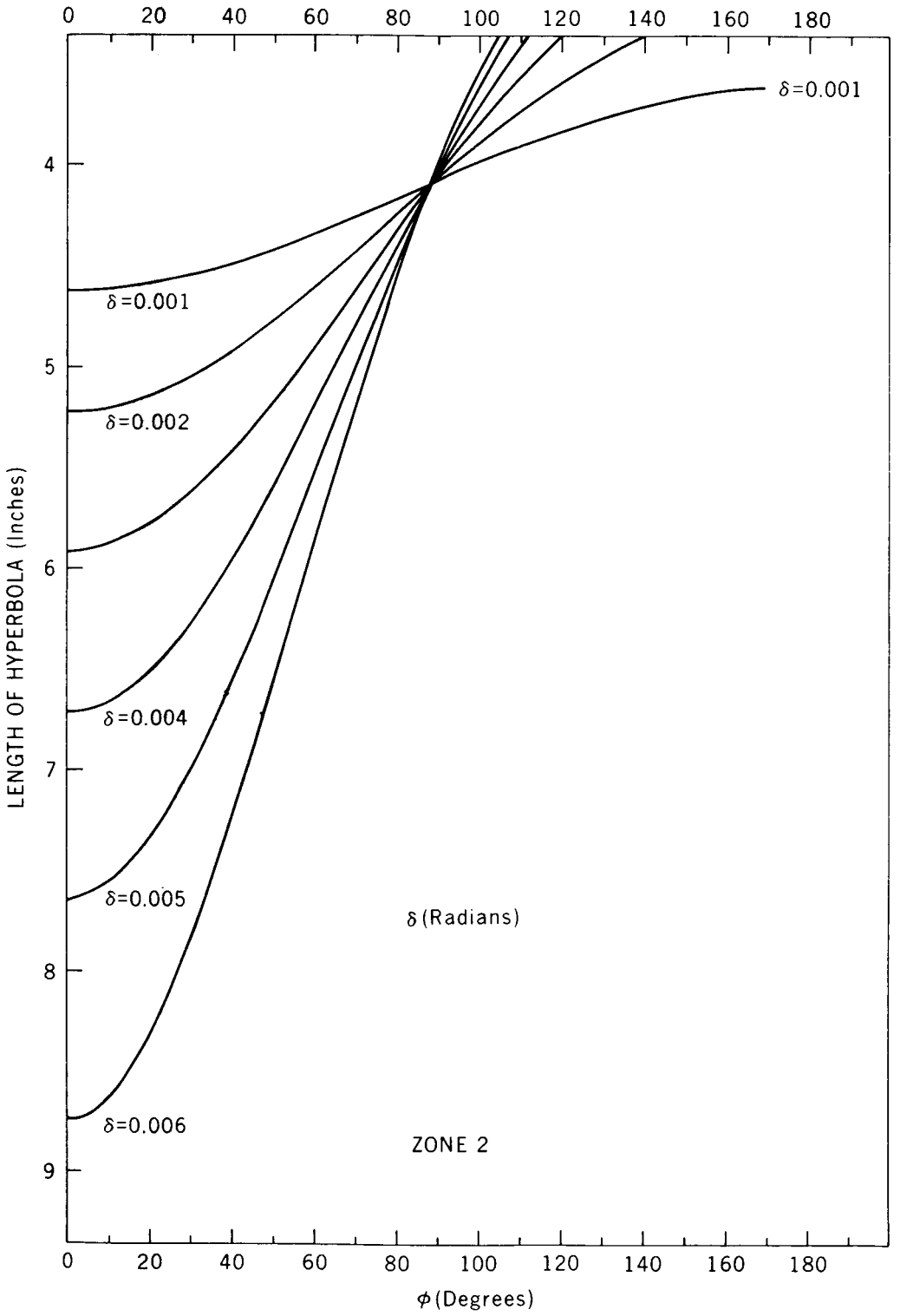

Figure 6B. Hyperbolic Intercept Versus Aperture Circumferential Angle

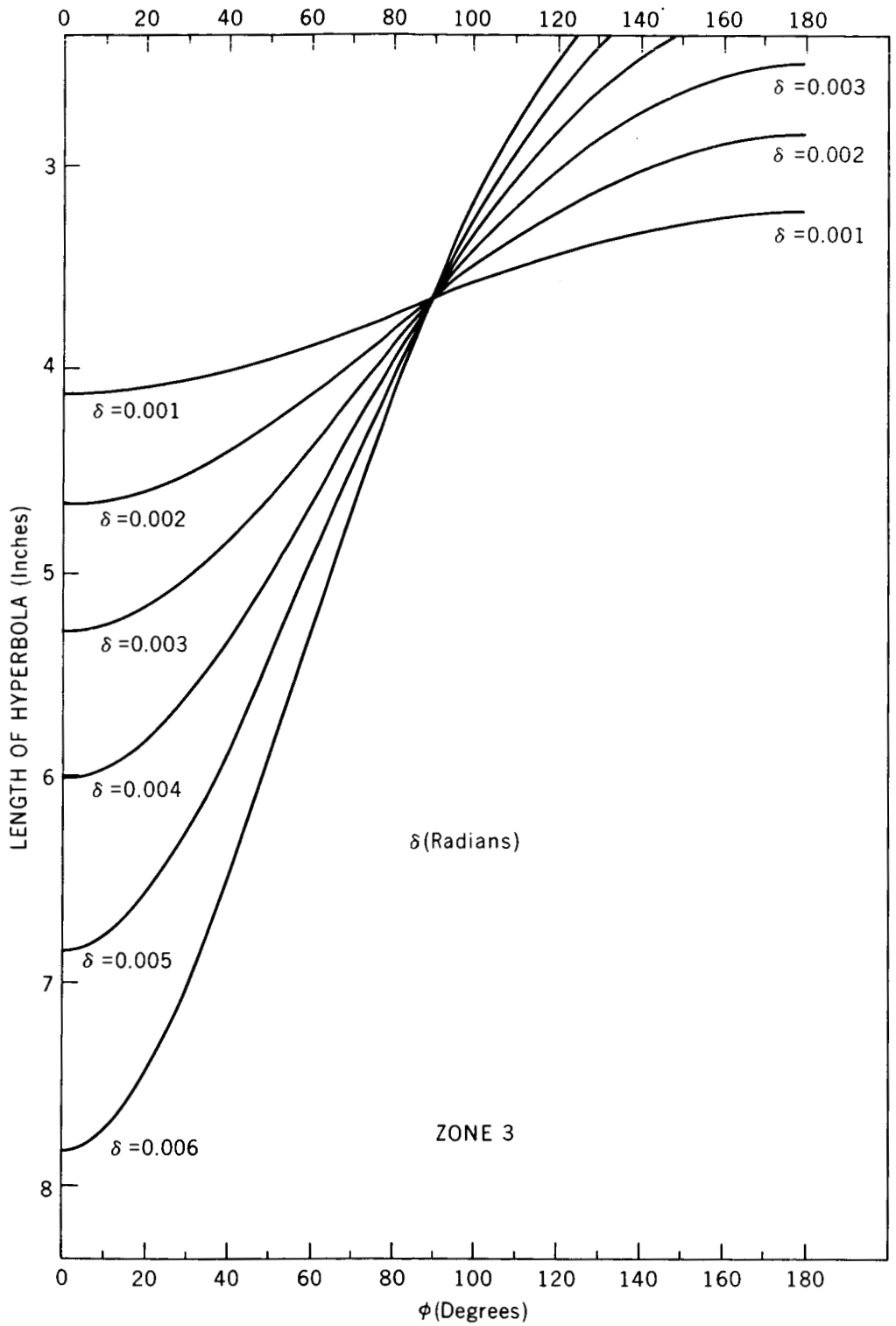

Figure 6C. Hyperbolic Intercept Versus Aperture Circumferential Angle

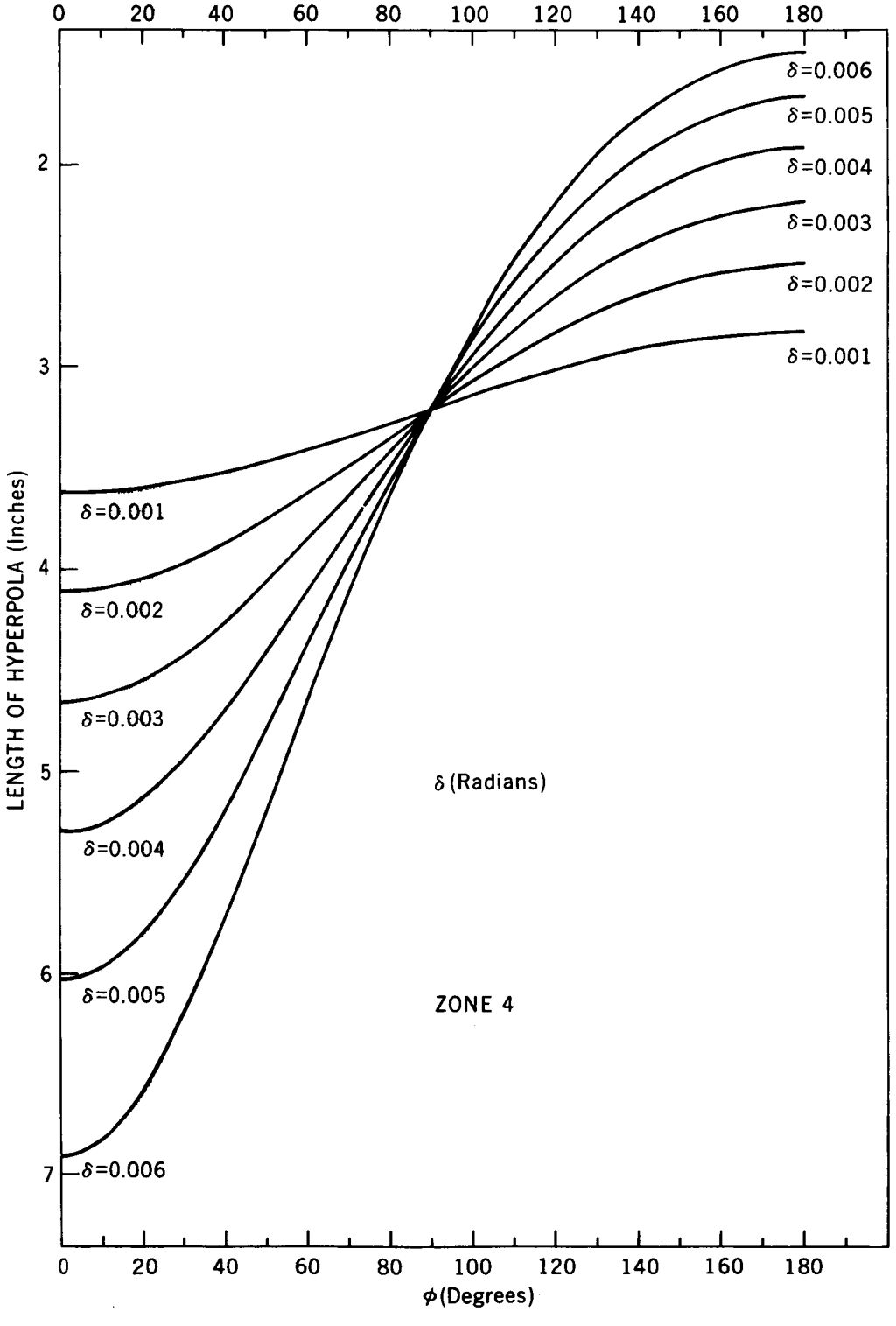

Figure 6D. Hyperbolic Intercept Versus Aperture Circumferential Angle

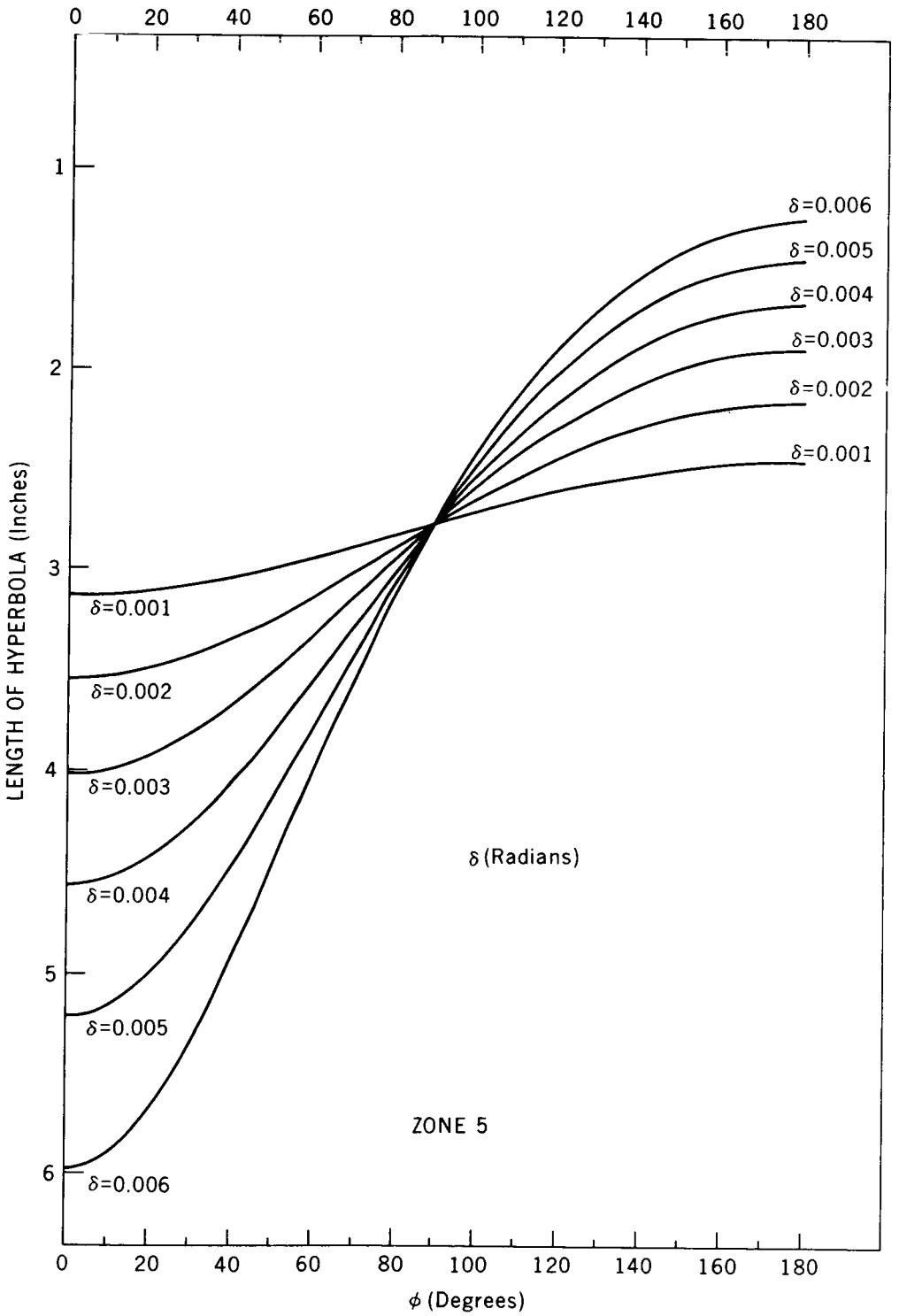

Figure 6E. Hyperbolic Intercept Versus Aperture Circumferential Angle

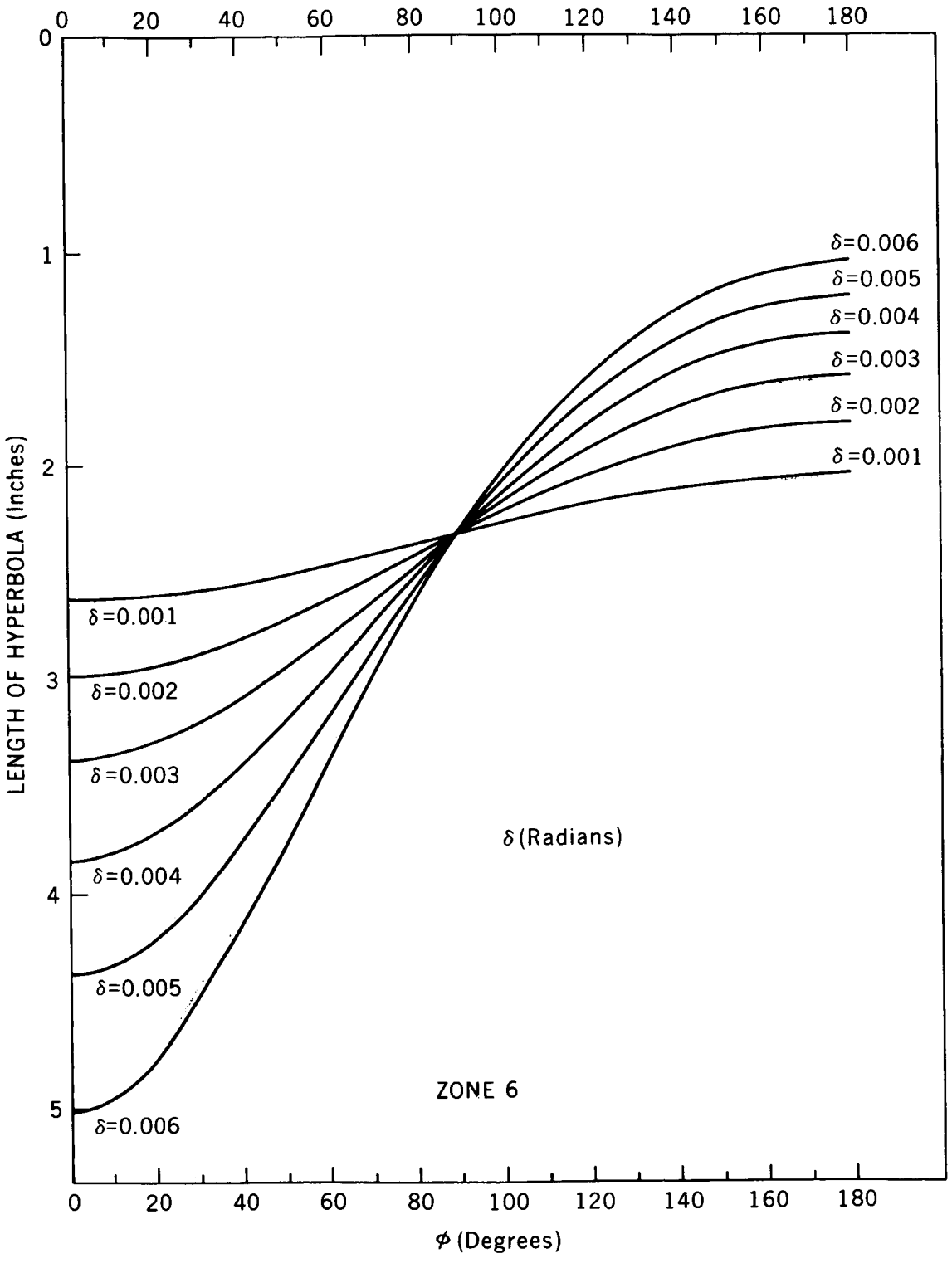

Figure 6F. Hyperbolic Intercept Versus Aperture Circumferential Angle

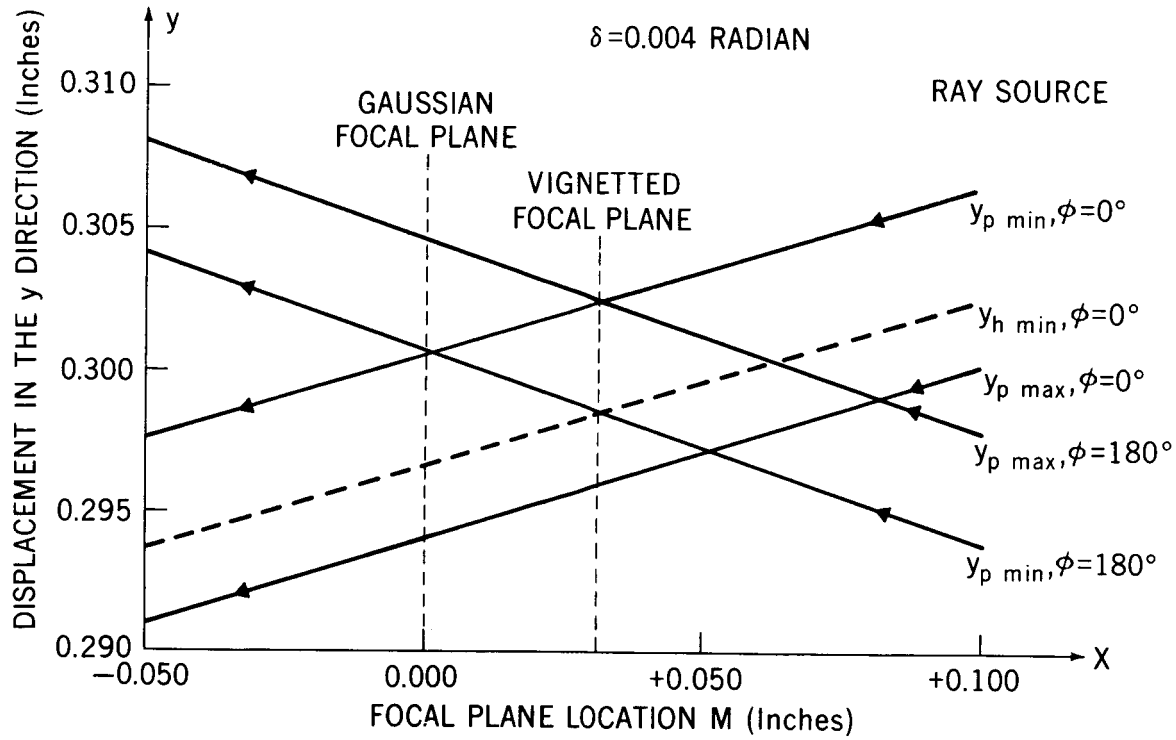

Figure 7. Displacement of Tangential Rays in XY Plane

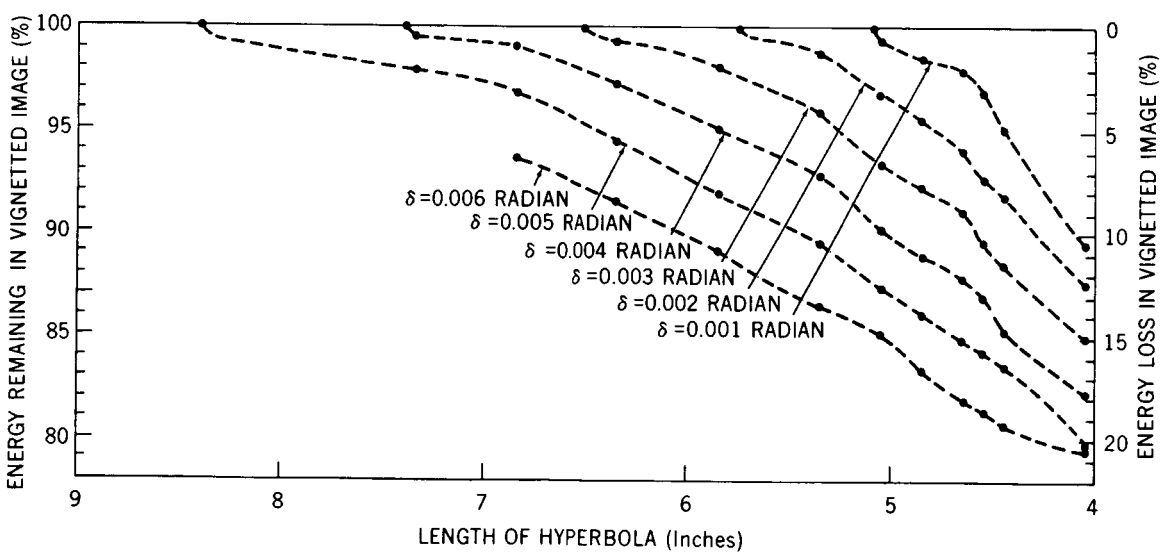

Figure 8. Energy Loss in Image of Point Source Versus Hyperbola Length

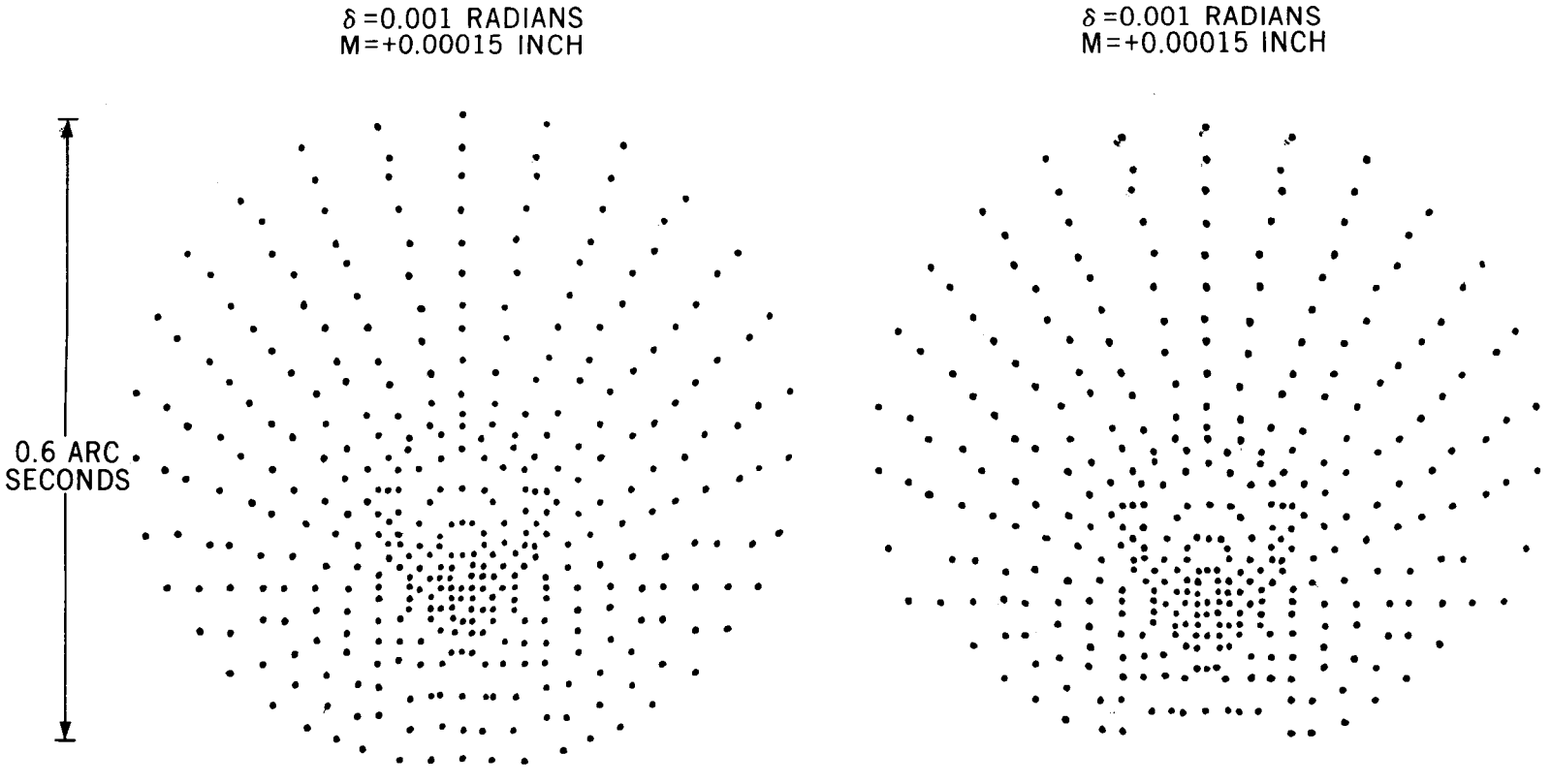

UNVIGNETTED
FIGURE 9A-1

VIGNETTED
FIGURE 9A-2

Figure 9A. Spot Diagram in Optimal Focal Position for Vignetted and Unvignetted Telescope

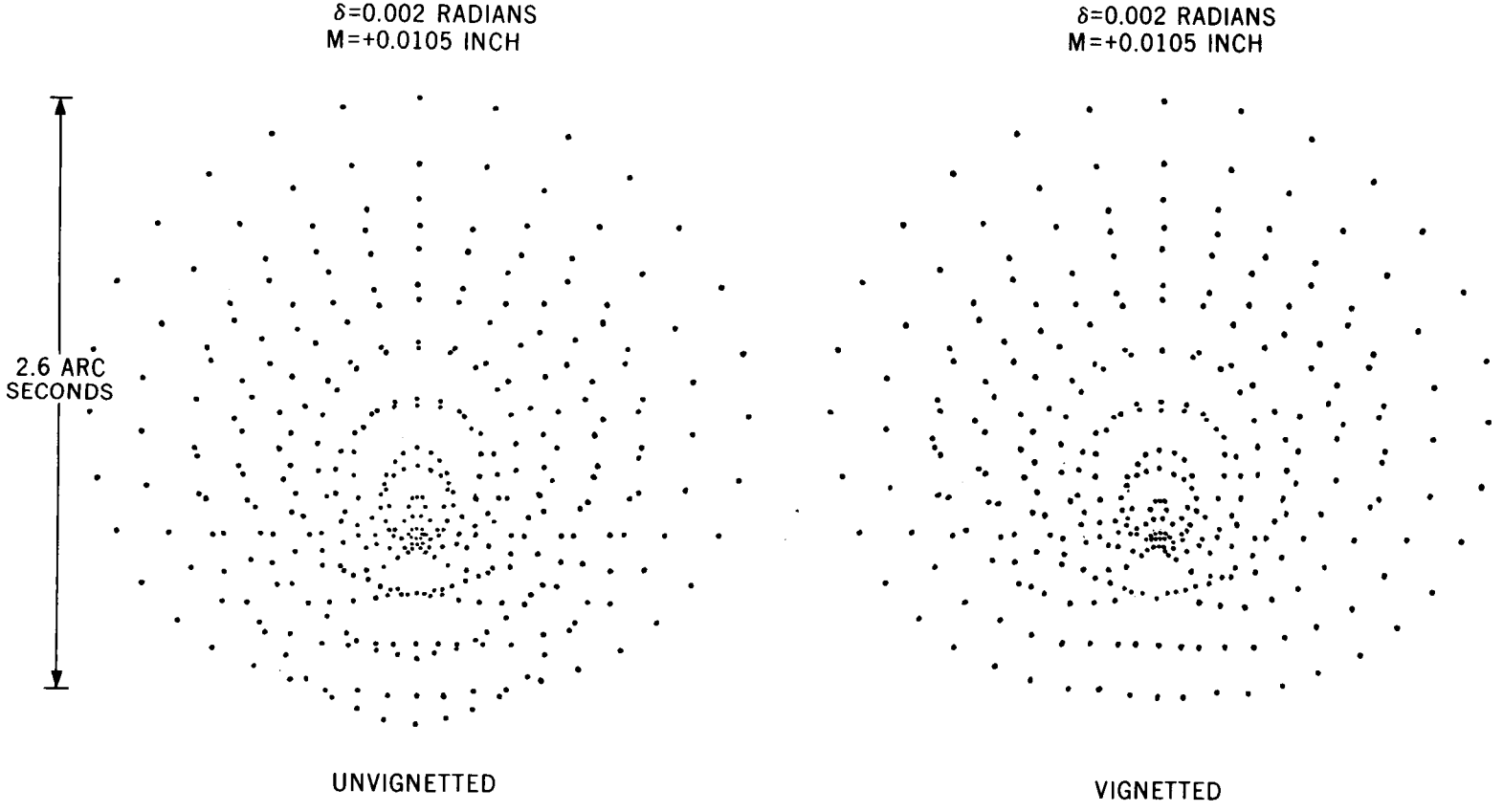

Figure 9B. Spot Diagram in Optimal Focal Position for Vignetted and Unvignetted Telescope

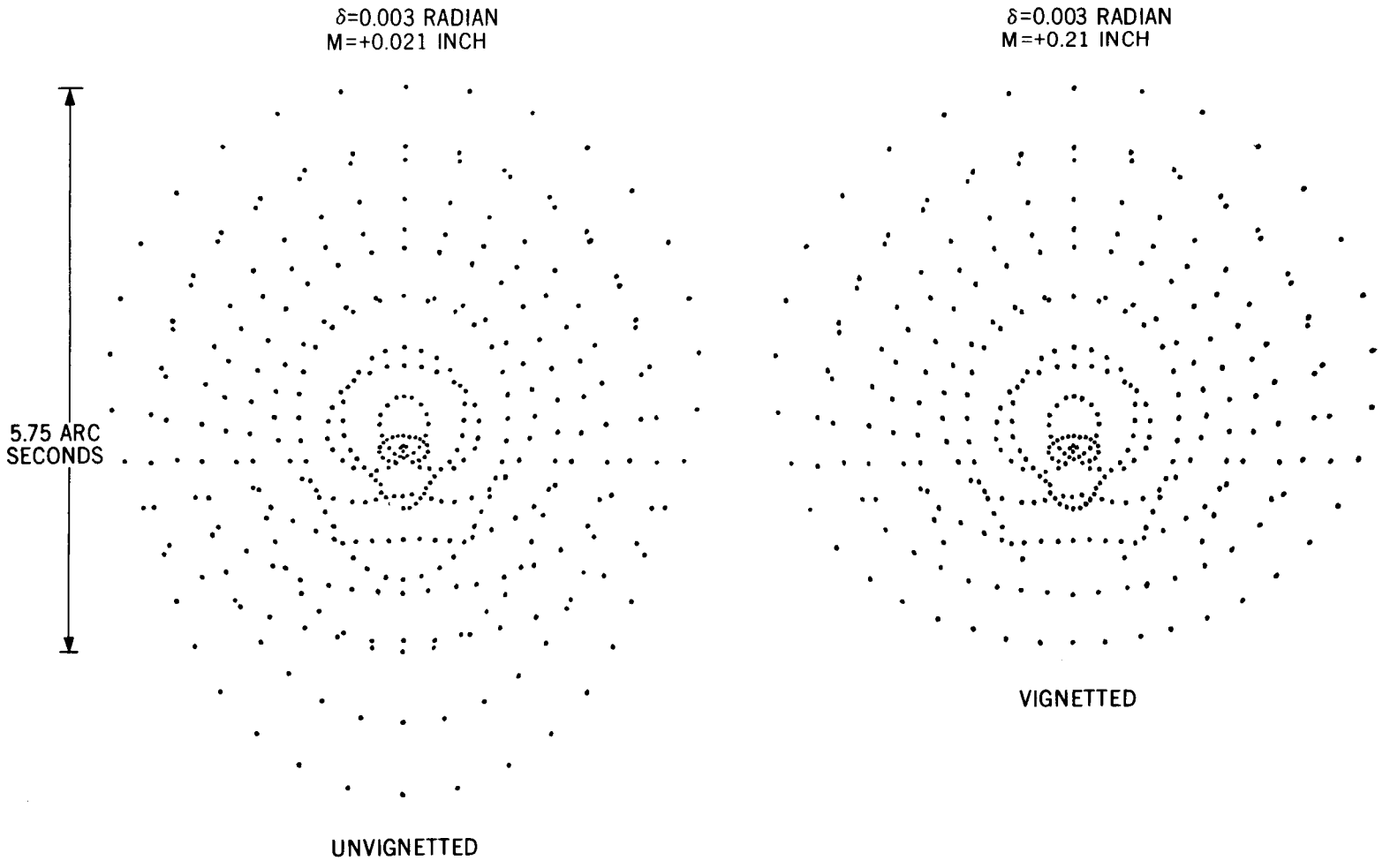

Figure 9C. Spot Diagram in Optimal Focal Position for Vignetted and Unvignetted Telescope

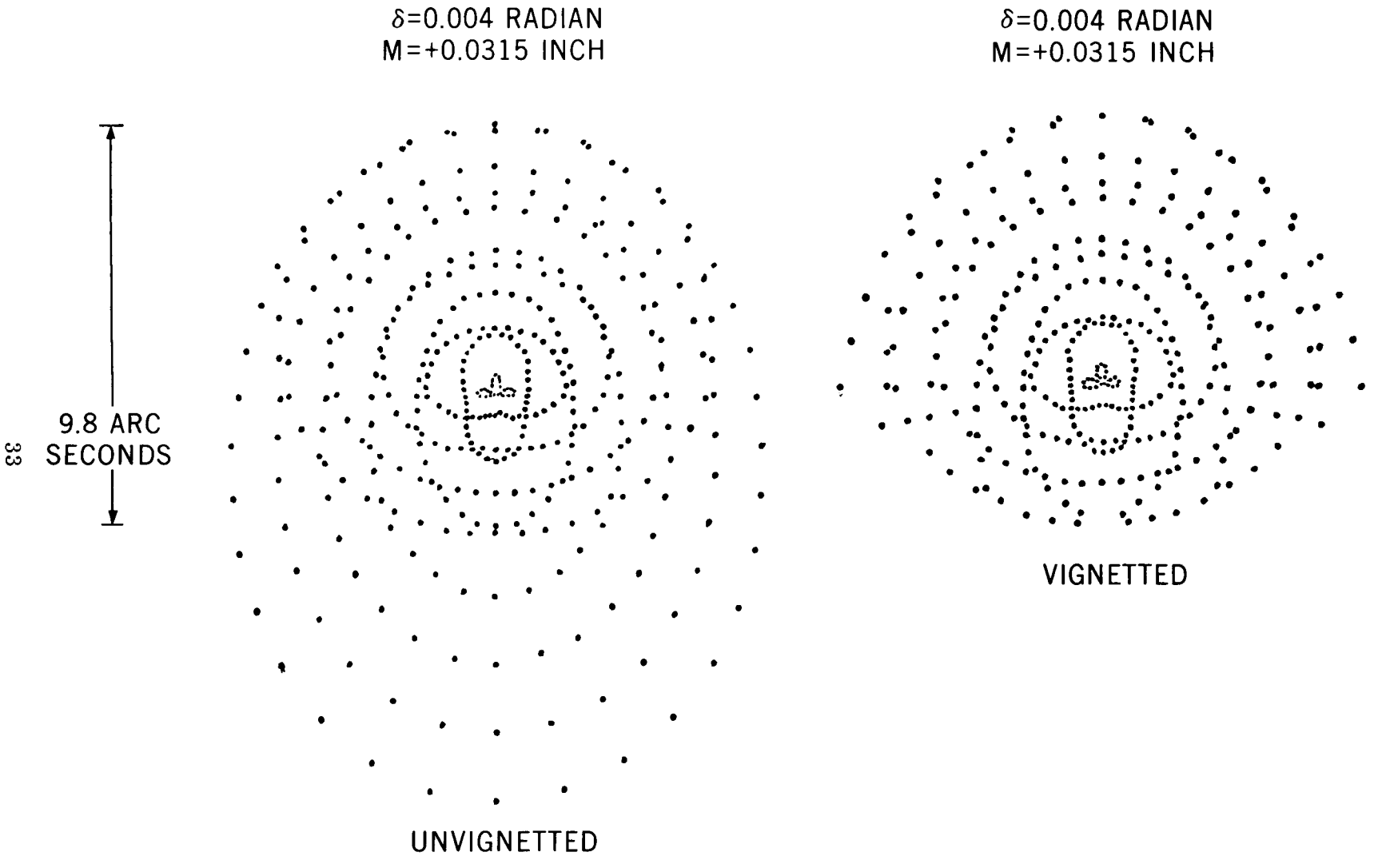

Figure 9D. Spot Diagram in Optimal Focal Position for Vignetted and Unvignetted Telescope

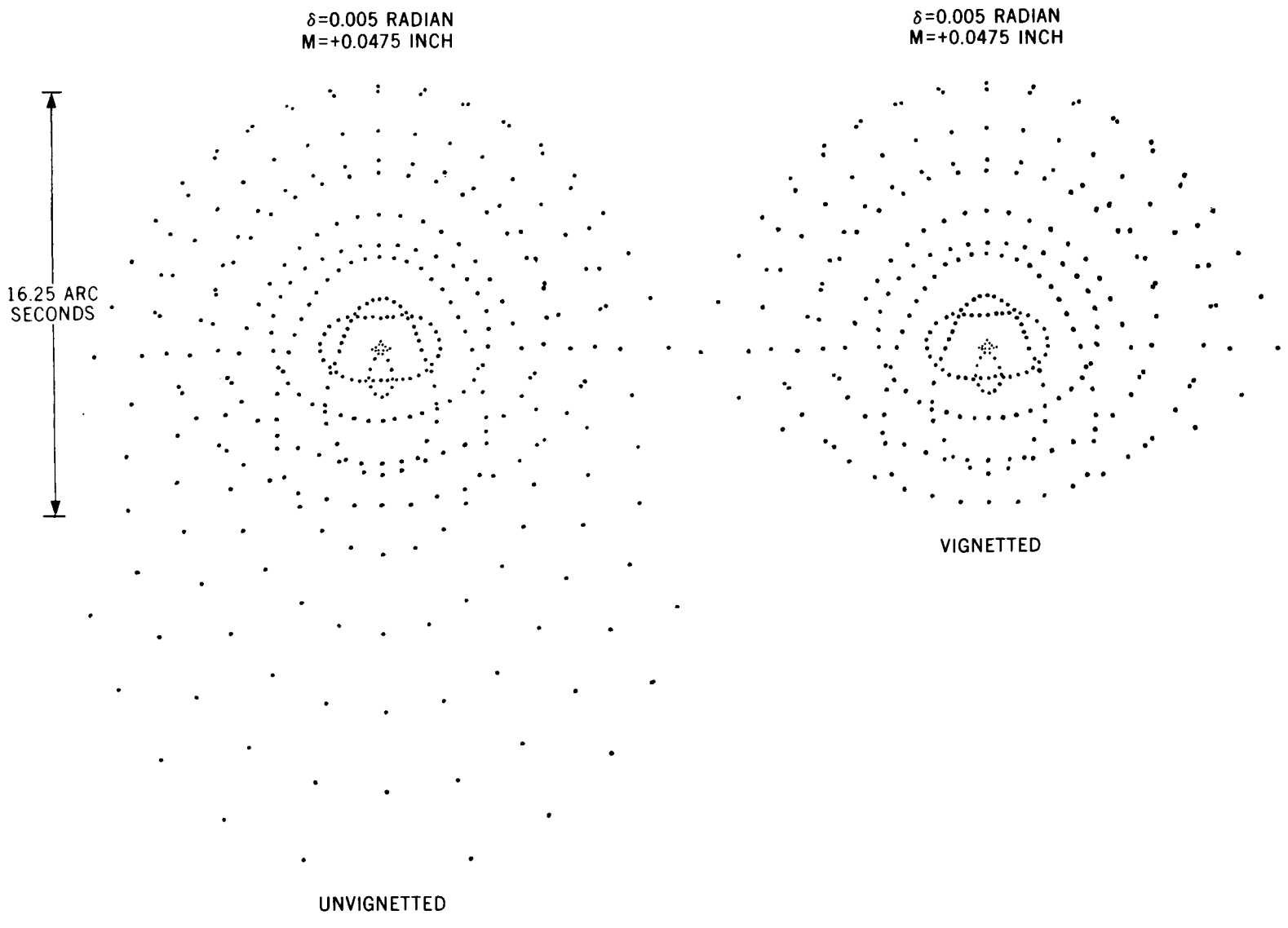

Figure 9E. Spot Diagram in Optimal Focal Position for Vignetted and Unvignetted Telescope

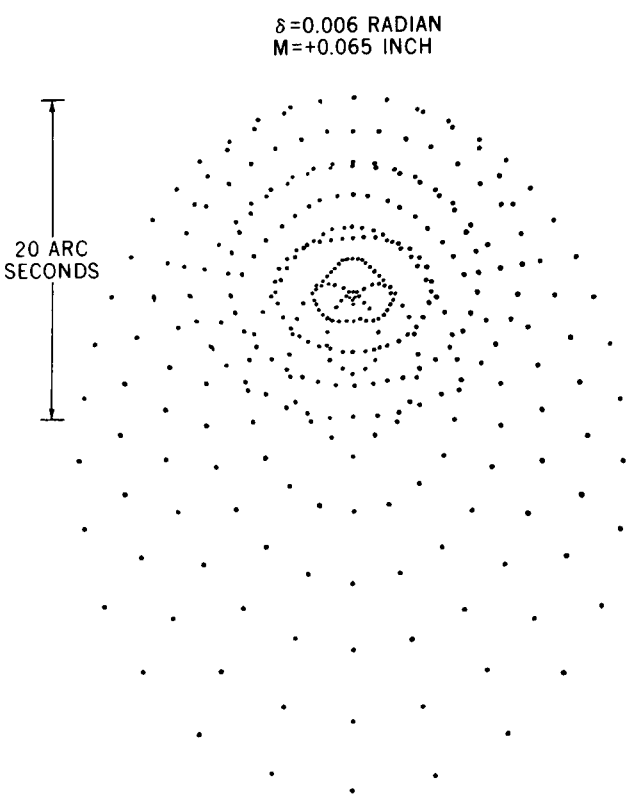

UNVIGNETTED
FIGURE 9F-1

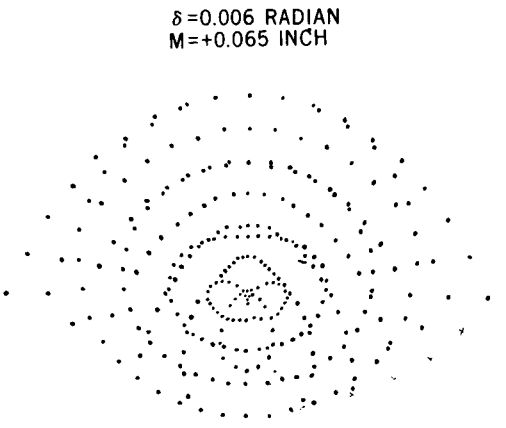

VIGNETTED
FIGURE 9F-2

Figure 9F. Spot Diagram in Optimal Focal Position for Vignetted and Unvignetted Telescope

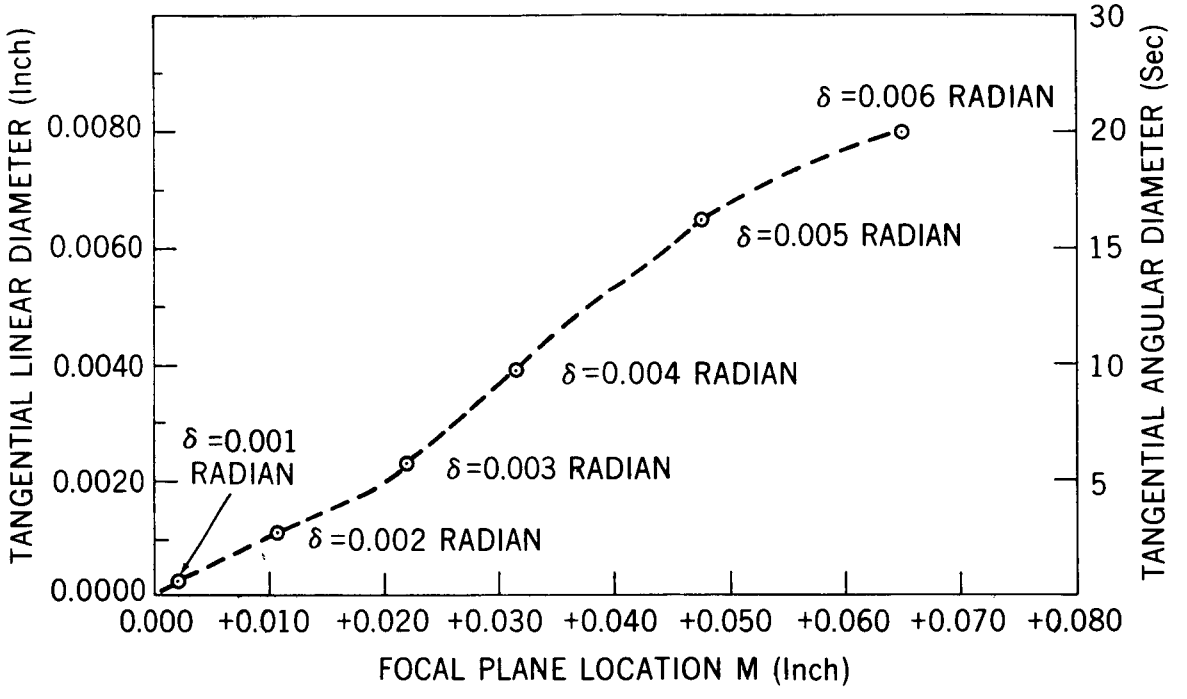

Figure 10. Optimal Focal Plane Locations of Vignetted Telescopes for Various Half Field Angles

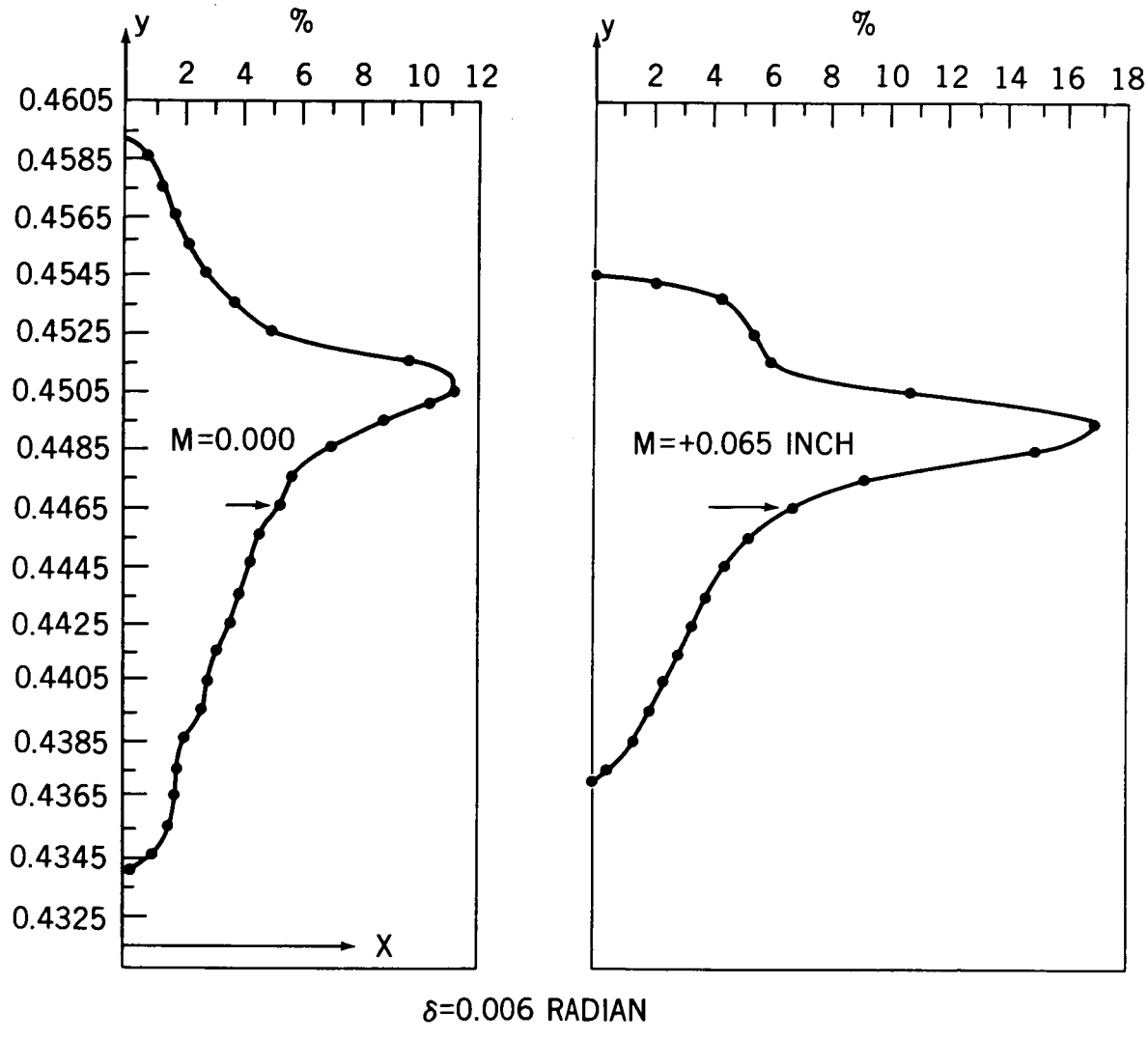

Figure 11A. Energy Distribution in Spot Diagrams at Gaussian and Optimal Focus

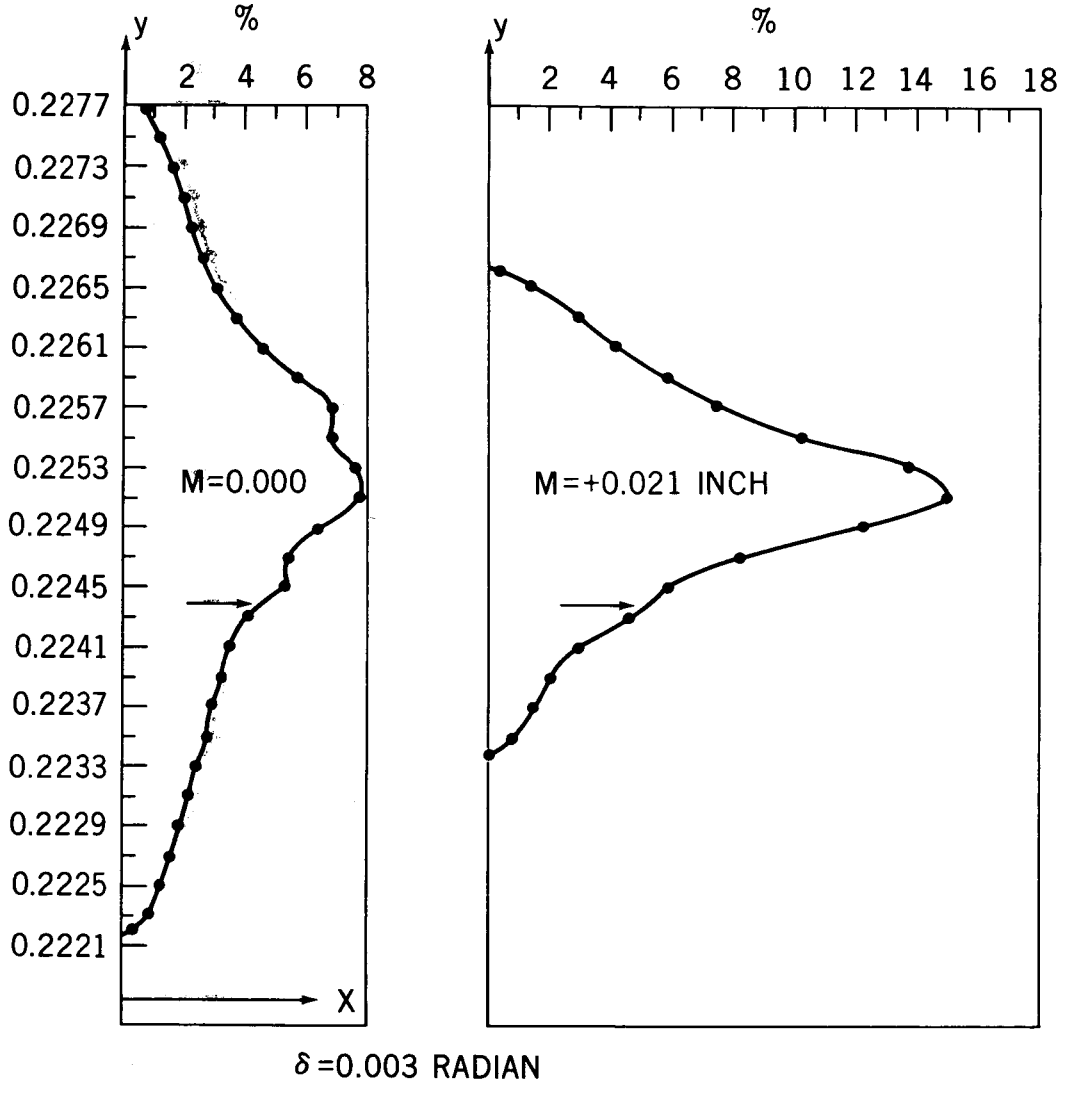

Figure 11B. Energy Distribution in Spot Diagrams at Gaussian and Optimal Focus

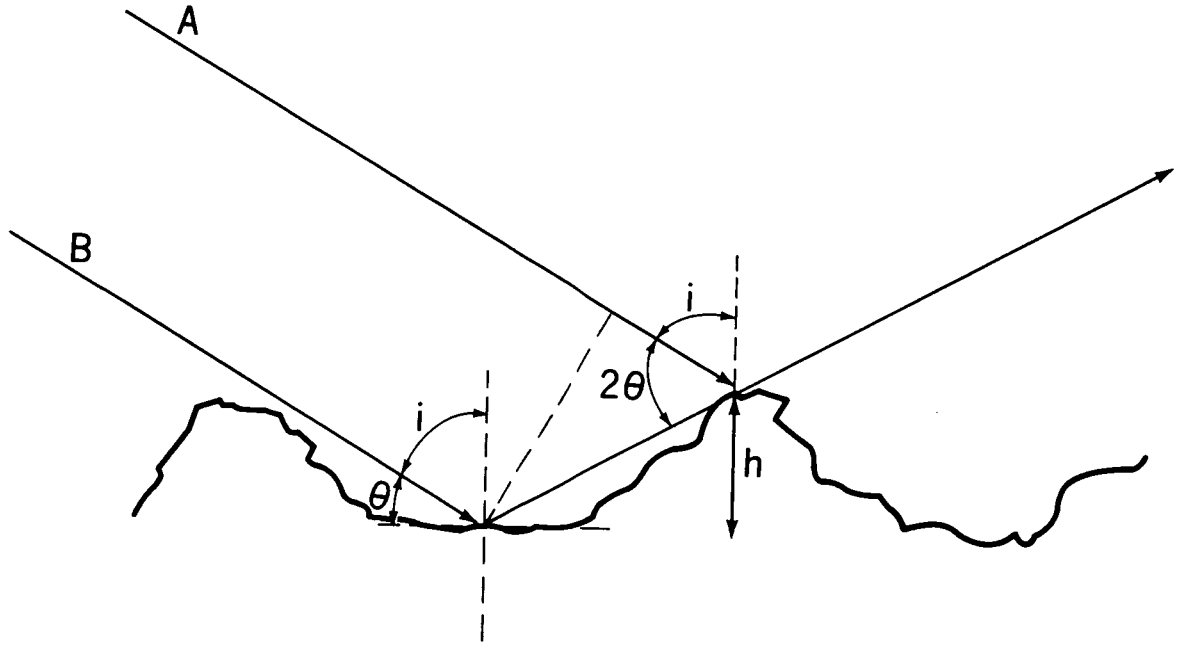

Figure 12. Reflection From a Rough Surface

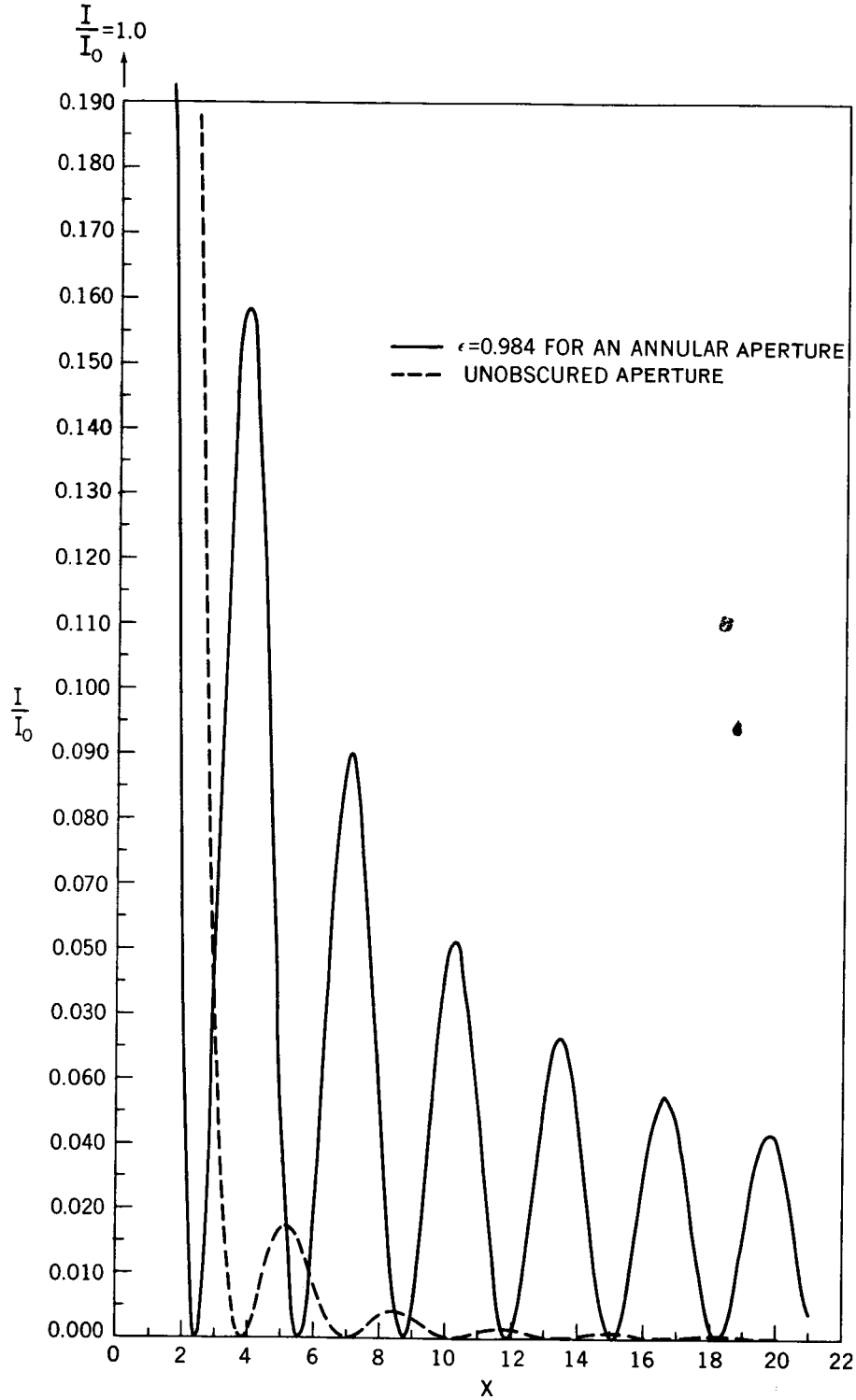

Figure 13. Diffraction by an Annular and Unobscured Aperture

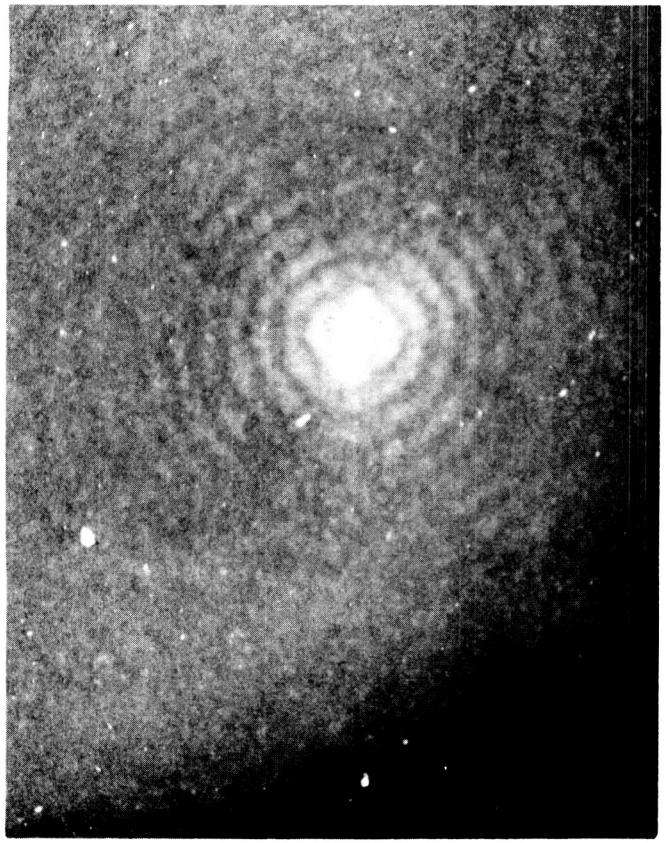

a.
ON AXIS IMAGE OF A 0.58
ARC SECOND SOURCE

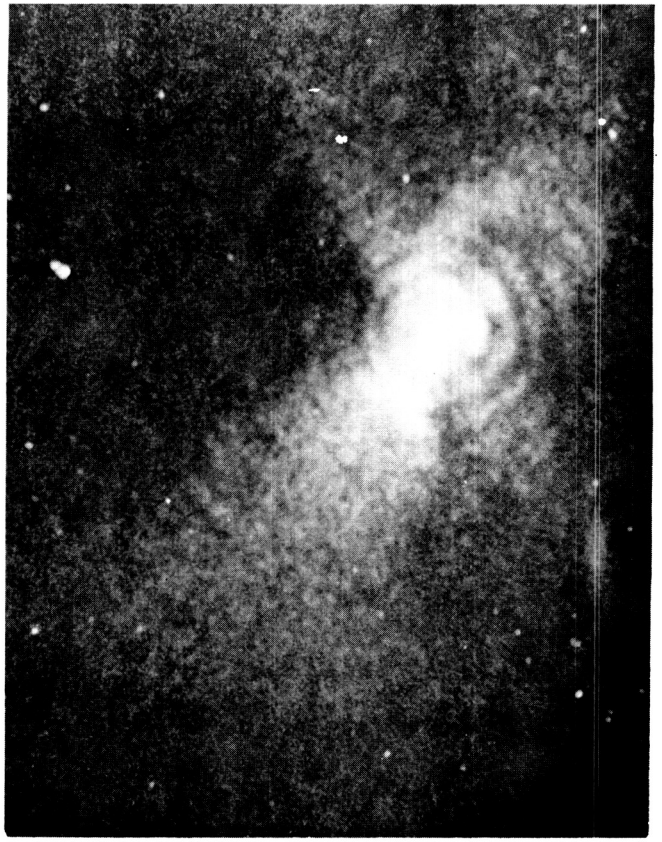

b.
0.50 DEGREE OFF AXIS
IMAGE OF A 0.58 ARC
SECOND SOURCE

Figure 14. Image of a Point Source Formed by an X-Ray Telescope

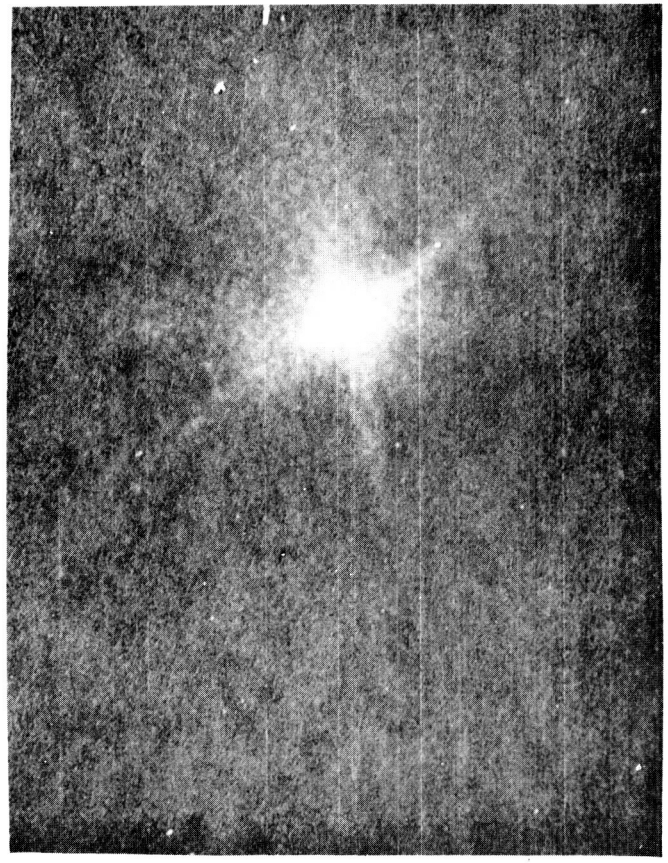

a.
ON AXIS IMAGE OF A 2.32
ARC SECOND SOURCE

b.
ON AXIS IMAGE OF A 5.79
ARC SECOND SOURCE

Figure 15. Image of Extended Sources Formed by an X-Ray Telescope

APPENDIX I

MATHEMATICAL DERIFICATION OF THE FUNDAMENTAL PARAMETERS OF A TYPE I X-RAY TELESCOPE

The basic parameters of a Type I x-ray telescope (concave parabola followed by a concave hyperbola) are derived using the notation in Figure 1. Rays A and B parallel to the optical axis x are incident at maximum and minimum points, respectively, defining the extent of the parabola aperture. The dashed lines which intersect the points (x_p, y_p) and $[(x_{p\,min}, y_{p\,min})$ or $(x_{h\,max}, y_{h\,max})]$ are drawn as tangent lines to the parabola and hyperbola with slope angles θ and θ_{max}, respectively.

If then one is given the maximum glancing angle θ_{max} for an incoming ray, the focal length f and the require collecting area A, the following parameters may then be calculated:

a, b, c, p, $y_{p\,min}$, $y_{h\,max}$, $x_{h\,max}$, $y_{p\,max}$, $x_{p\,max}$, θ_{min}, $y_{h\,min}$, $x_{h\,min}$

where the parabola is given by

$$y_p^2 = p(2x_p + p)$$

and the hyperbola by

$$\frac{(x_h - c)^2}{a^2} - \frac{y^2}{b^2} = 1$$

For $y_{p\,min}$: $y_{p\,min} = f \sin 4\theta_{max}$

For p : $p = y_{p\,min} \tan \theta_{max}$

For $x_{p\,min}$: $\tan 2\theta_{max} = \dfrac{y_{p\,min}}{x_{p\,min}}$

$$x_{p\,min} = 2 f^2 \cos^2 2\theta_{max}$$

For a : $$a = \frac{y_{p\,min}}{2}\left[\frac{1}{\sin 2\theta_{max}} - \frac{1}{\sin 4\theta_{max}}\right]$$

$$a = \frac{f}{2}(2\cos 2\theta_{max} - 1)$$

For c : $$c = \frac{1}{2}\left[x_{p\,min} - f\cos 4\theta_{max}\right]$$

$$c = \frac{f}{2}$$

For b : $$b = (c^2 - a^2)^{1/2}$$

For $x_{h\,max}$: $$x_{h\,max} = x_{p\,min}$$

For $y_{h\,max}$: $$y_{h\,max} = y_{p\,min}$$

For $y_{p\,max}$: $$A = \pi\left(y^2_{p\,max} - y^2_{p\,min}\right)$$

$$y_{p\,max} = \left[\frac{A}{\pi} + y^2_{p\,min}\right]^{1/2}$$

For $x_{p\,max}$: $$y^2_{p\,max} = p(2x_{p\,max} + p)$$

$$x_{p\,max} = \frac{1}{2}\left[\frac{y^2_{p\,max}}{p} - p\right]$$

For θ_{min} : $$\tan\theta_{min} = \frac{p}{y_{p\,max}}$$

$$\theta_{min} = \tan^{-1} \frac{p}{y_{p\,max}}$$

For $y_{h\,min}$: $$y_{h\,min} = \frac{\frac{x_{p\,max}}{y_{p\,max}} c \pm \left[\left(\frac{x_{p\,max}}{y_{p\,max}} \right)^2 (1 - b^2) + a^2 \right]^{1/2}}{\frac{a^2}{b^2} - \frac{x_{p\,max}^2}{y_{p\,max}^2}}$$

For $x_{h\,min}$: $$x_{h\,min} = \frac{x_{p\,max}}{y_{p\,max}} y_{h\,min}$$

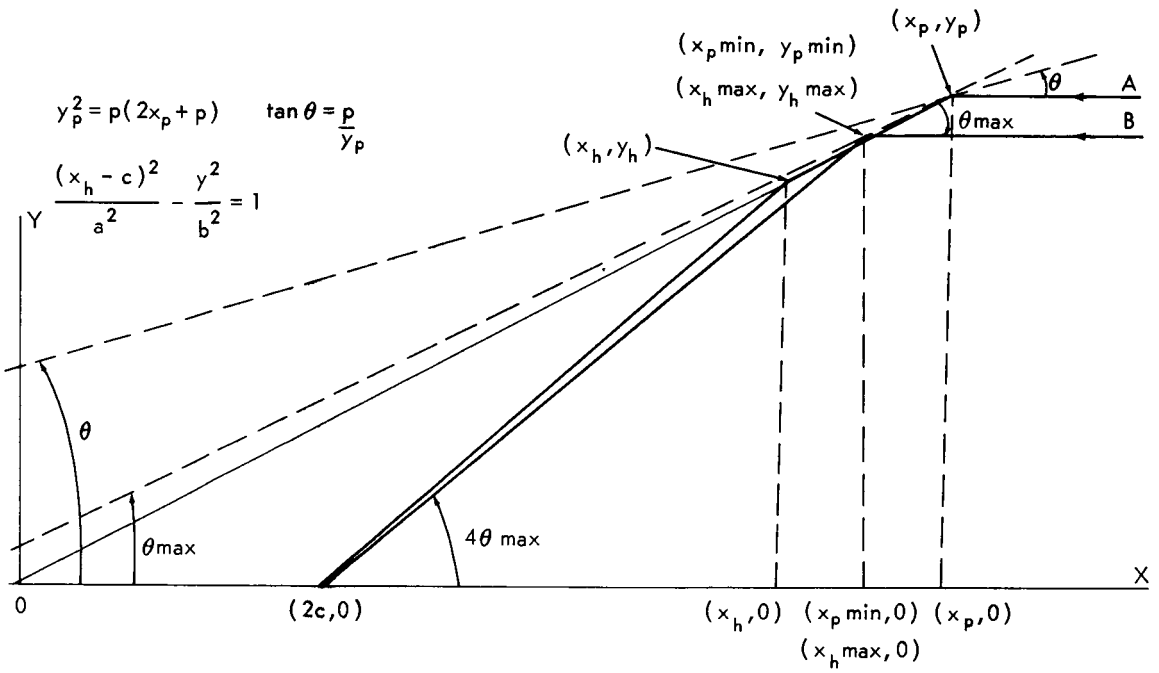
$y_p^2 = p(2x_p + p)$
$\tan\theta = \frac{p}{y_p}$
$\frac{(x_h - c)^2}{a^2} - \frac{y^2}{b^2} = 1$
(x_p, y_p)
$(x_p \min,\ y_p \min)$
$(x_h \max,\ y_h \max)$
(x_h, y_h)
θ
$\theta \max$
A
B
Y
X
θ
$\theta \max$
$4\theta \max$
0
$(2c, 0)$
$(x_h, 0)$
$(x_p \min, 0)$
$(x_h \max, 0)$
$(x_p, 0)$

Figure 1

APPENDIX II

ELEMENTS OF THE RAY TRACE PROCEDURE FOR TYPE I AND TYPE II X-RAY TELESCOPES

Rays incident on the circumference of the parabolic element are considered to lie in the XY plane and make an angle delta, δ, with the XZ plane as shown in Figure 1.

The location of the point of intersection P (x, y, z) of the ray with the aperture is given by the angle phi, ϕ, as measured from the Y axis. Before tracing the ray through the system, the point P (x, y, z) is rotated through the angle ϕ until it is coincident with the point P (x_1', y_1, z_1) on the Y axis. The angles formed by the incident ray with the XY plane and XZ plane are denoted as δ_s and δ_t, respectively. These angles, δ_s and δ_t, are calculated as shown in Figures 4 and 5.

It is necessary to determine the above angles since the direction cosines of the ray striking P (x_1', y_1, z_1) are calculated as follows from Figures 2 and 3.

For the case of $0° \leq \phi \leq 90°$

$$\cos \alpha = \cos (180° - \delta) = - \cos \delta$$

$$\cos \beta = \cos (90° - \delta_t) = \sin \delta_t$$

$$\cos \gamma = \cos (90° + \delta_s) = - \sin \delta_s$$

and for the case of $90° < \phi \leq 180°$

$$\cos \alpha = \cos (180° + \delta) = - \cos \delta$$

$$\cos \beta = \cos (90° + \delta_t) = - \sin \delta_t$$

$$\cos \gamma = \cos (90° + \delta_s) = - \sin \delta_s$$

Figures 4 and 5 have been drawn for the cases when the point P (x, y, z) is located in the quadrant $0° \leq \phi \leq 90°$ and $90° < \phi \leq 180°$. It is seen from Figure 4 that for $0° \leq \phi \leq 90°$

$$\sin \delta = \frac{AB}{N} \qquad AB = N \sin \delta$$

$$\sin \delta_s = \frac{AC}{N} \qquad AC = N \sin \delta_s$$

$$\sin \phi = \frac{AC}{AB} \qquad AC = AB \sin \phi = N \sin \delta \sin \phi$$

$$\therefore \sin \delta_s = \sin \delta \sin \phi$$

$$\sin \delta_t = \frac{AD}{N} \qquad AD = N \sin \delta_t$$

$$\cos \phi = \frac{AD}{AB} \qquad AD = AB \cos \phi = N \sin \delta \cos \phi$$

$$\therefore \sin \delta_t = \sin \delta \cos \phi$$

and from Figure 5 that for $90° < \phi \leq 180°$

$$\sin \delta = \frac{AB}{N} \qquad AB = N \sin \delta$$

$$\sin \delta_s = \frac{AD}{N} \qquad AD = N \sin \delta_s$$

$$\sin (180° - \phi) = \frac{AD}{AB} \qquad AD = AB \sin \phi = N \sin \delta \sin \phi$$

$$\therefore \sin \delta_s = \sin \delta \sin \phi$$

$$\sin \delta_t = \frac{AC}{N} \qquad AC = N \sin \delta_t$$

$$\cos (180° - \phi) = \frac{BD}{AB} = \frac{AC}{AB} \qquad AC = -AB \cos \phi = -N \sin \delta \cos \phi$$

$$\therefore \sin \delta_t = -\sin \delta \cos \phi$$

It should be noted that sin δ_t may be considered in the form sin δ_t = sin δ cos ϕ since cos ϕ is positive for $0° \leq \phi \leq 90°$ and negative for $90° < \phi \leq 180°$.

The next parameters to be determined are the direction cosines of the surface normal to the point $P(x'_1, y_1, z_1)$. The surface normal is denoted by N_1 as shown in Figure 6. The slope of the tangent to the point $P(x'_1, y_1, z_1)$ is defined as $\alpha_1/2$. Calculation of the direction cosines is then as follows:

$$\cos \alpha = \cos \left(90° - \frac{\alpha_1}{2}\right) = \sin \frac{\alpha_1}{2} = \frac{x}{N_1}$$

$$\cos \beta = \cos \left(180° - \frac{\alpha_1}{2}\right) = -\cos \frac{\alpha_1}{2} = \frac{y}{N_1}$$

Hence:

$$x = N_1 \sin \frac{\alpha_1}{2}$$

$$y = -N_1 \cos \frac{\alpha_1}{2}$$

The direction cosines of the surface normal are then:

$$\left(\sin \frac{\alpha_1}{2}, -\cos \frac{\alpha_1}{2}, 0\right)$$

if N_1 is considered to be a unit vector. It is clear from Figure 6 that α_1 may be calculated from the relationship

$$\alpha_1 = \tan^{-1}\left(\frac{y_1}{x'_1}\right)$$

where

$$y_1 = \left[p(2x_1' + p)\right]^{1/2}.$$

Direction cosines defining the reflected vector, S_1, are then calculated by using the equation:

$$S_1 = S_o - 2N_1 (S_o N_1)$$

where the direction cosines have been shown to be S_o $(-\cos \delta, \sin \delta_t, -\sin \delta_s)$ for the incident vector and $N_1 \left(\sin \frac{\alpha_1}{2}, -\cos \frac{\alpha_1}{2}, 0\right)$ for the surface normal. Substitution of these directional components into S_1 yields

$$S_1 = -\cos \delta \, \bar{i} + \sin \delta_t \, \bar{j} - \sin \delta_s \, \bar{k} - 2 \left[\sin \frac{\alpha_1}{2} \, \bar{i} - \cos \frac{\alpha_1}{2} \, \bar{j} + 0 \, \bar{k}\right]$$

$$x \left[(-\cos \delta \, \bar{i} + \sin \delta_t \, \bar{j} - \sin \delta_s \, \bar{k}) \left(\sin \frac{\alpha_1}{2} \, \bar{i} - \cos \frac{\alpha_1}{2} \, \bar{j} + 0 \, \bar{k}\right)\right]$$

After vector multiplication and collecting terms

$$S_1 = (\sin \delta_t \sin \alpha_1 - \cos \delta \cos \alpha_1) \, \bar{i}$$

$$+ (-\sin \delta_t \cos \alpha_1 - \cos \delta \sin \alpha_1) \, \bar{j} - \sin \delta_s \, \bar{k}$$

The direction cosine's defining the reflected vector are then denoted as

$$S_{1x} = \sin \delta_t \sin \alpha_1 - \cos \delta \cos \alpha_1$$

$$S_{1y} = -\sin \delta_t \cos \alpha_1 - \cos \delta \sin \alpha_1$$

$$S_{1z} = -\sin \delta_s$$

This reflected ray is then incident at point $P(x_2', y_2, z_2)$ on the hyperbolic surface which has the form, in the present coordinate system, of

$$\frac{(x'_2 - c)^2}{a^2} - \frac{y^2}{b^2} - \frac{z^2}{b^2} = 1$$

For the case of the Type I telescope, a concave parabolic mirror followed by a concave hyperbolic mirror, the above equation is correct. However, for the Type II telescope, a concave parabolic mirror followed by a convex hyperbolic mirror, the hyperbolic surface is described by

$$\frac{(x'_2 + c)^2}{a^2} - \frac{y^2}{b^2} - \frac{z^2}{b^2} = 1$$

It is convenient to perform the linear transformation

$$x_1 = x'_1 - c$$

$$x_2 = x'_2 - c$$

since now the hyperbolic element of both types of telescopes is described by

$$\frac{x_2^2}{a^2} - \frac{y_2^2}{b^2} - \frac{z_2^2}{b^2} = 1$$

The computer program must consider the value c as multiplied by -1 in order to perform the proper transformation for the Type II telescope.

Now it is necessary to calculate, ℓ_2, the magnitude of the vector between points $P(x_1, y_1, z_1)$ and $P(x_2, y_2, z_2)$ as illustrated in Figure 7. The angle θ is used as an arbitrary supplementary angle in deriving the following equations:

$$S_{1x} = \cos \alpha = \cos (180° + \theta) = -\cos \theta = -\left(\frac{x_1 - x_2}{\ell_2}\right)$$

$$x_2 = x_1 + \ell_2 S_{1x}$$

$$S_{1y} = \cos \beta = \cos (90° + \theta) = - \sin \theta = -\left(\frac{y_1 - y_2}{\ell_2}\right)$$

$$y_2 = y_1 + \ell_2 S_{1y}$$

$$S_{1z} = \cos \gamma = \cos (90° + \theta) = - \sin \theta = -\left(\frac{0 - z_2}{\ell_2}\right)$$

$$z_2 = \ell_2 S_{1z}$$

Substitution of these equalities into the hyperbolic surface equation has the form

$$\frac{(x_1 + \ell_2 S_{1x})^2}{a^2} - \frac{(y_1 + \ell_2 S_{1y})^2}{b^2} - \frac{(\ell_2 S_{1z})^2}{b^2} = 1$$

By expanding and collecting terms one has

$$\ell_2^2 \left[\left(\frac{c}{a}\right)^2 S_{1x}^2 - 1\right] - 2\ell_2 \left[y_1 S_{1y} - \left(\frac{b}{a}\right)^2 x_1 S_{1x}\right]$$

$$+ \left[\left(\frac{b}{a}\right)^2 x_1^2 - y_1^2 - b^2\right] = 0$$

or

$$\ell_2 = \frac{B_2 \pm (B_2^2 - A_2 C_2)^{1/2}}{A_2}$$

\- root for Type I

\+ root for Type II

where

$$A_2 = \left(\frac{c}{a}\right)^2 S_{1x}^2 - 1$$

$$B_2 = y_1 S_{1y} - \left(\frac{b}{a}\right)^2 x_1 S_{1x}$$

$$C_2 = \left(\frac{b}{a}\right)^2 x_1^2 - y_1^2 - b^2$$

The next step is to determine the direction cosines of the normal to the hyperbolic surface. The quantity, N_2, is defined as the magnitude of the surface normal between point P (x_2, y_2, z_2) and where it intersects the X axis. This axial intersection takes place because the hyperbola is a surface of revolution. The X intercept is calculated from Figure 8 as follows. The equation for the hyperbola is written in the form

$$F(x_2, y_2, z_2) = \frac{x_2^2}{a^2} - \frac{y_2^2}{b^2} - \frac{z_2^2}{b^2} - 1 = 0$$

since the equation of the normal may be determined by the general relationship

$$\frac{x - x_2}{\frac{\partial F(x_2, y_2, z_2)}{\partial x_2}} = \frac{y - y_2}{\frac{\partial F(x_2, y_2, z_2)}{\partial y_2}} = \frac{z - z_2}{\frac{\partial F(x_2, y_2, z_2)}{\partial z_2}}$$

if

$$F(x_2, y_2, z_2) = 0$$

Therefore,

$$\frac{\partial F}{\partial x_2} = \frac{2x_2}{a^2}$$

$$\frac{\partial F}{\partial y_2} = \frac{2y_2}{-b^2}$$

$$\frac{\partial F}{\partial z_2} = \frac{2z_2}{-b^2}$$

and the equation of the normal to P (x_2, y_2, z_2) is determined to be

$$\frac{x - x_2}{x_2} a^2 = \frac{y - y_2}{-y_2} b^2 = \frac{z - z_2}{-z_2} b^2$$

The X intercept of the surface normal with the optical axis is thus found to be

$$x = \frac{b^2}{a^2} x_2 + x_2 \qquad y = 0$$

The magnitude of N_2 is given by

$$N_2^2 = y_2^2 + x_2^2 \frac{b^4}{a^4} + z_2^2$$

however

$$y_2^2 + z_2^2 = \frac{b^2}{a^2} x_2^2 - b^2$$

and by substitution

$$N_2 = \frac{b x_2}{a} \left[\left(\frac{c}{a} \right)^2 - \left(\frac{a}{x_2} \right)^2 \right]^{1/2}$$

$$T \equiv \frac{1}{N_2}$$

The direction cosines of N_2 are then determined from Figure 8 and once again θ is used as an arbitrary supplemental angle.

$$N_{2x} = \cos \alpha = \cos (90° - \theta) = \sin \theta = \frac{x_2 + x_2 \left(\frac{b^2}{a^2} \right) - x_2}{N_2}$$

$$N_{2x} = x_2 \left(\frac{b}{a} \right)^2 T$$

$$N_{2y} = \cos \beta = \cos (180° - \theta) = \cos \theta = -\frac{y_2}{N_2}$$

$$N_{2y} = - y_2 T$$

$$N_{2z} = \cos \gamma = \frac{0 - z_2}{N_2}$$

$$N_{2z} = - z_2 T$$

The direction cosines of the ray reflected from the hyperbola are again determined from the relationship

$$S_2 = S_1 - 2 N_2 (S_1 N_2)$$

which becomes

$$S_2 = S_{1x}\,\bar{i} + S_{1y}\,\bar{j} + S_{1z}\,\bar{k} - 2\,(N_{2x}\,\bar{i} + N_{2y}\,\bar{j} + N_{2z}\,\bar{k})$$

$$\left[(S_{1x}\,\bar{i} + S_{1y}\,\bar{j} + S_{1z}\,\bar{k})\ \ (N_{2x}\,\bar{i} + N_{2y}\,\bar{j} + N_{2z}\,\bar{k})\right]$$

$$S_2 = S_{1x}\,\bar{i} + S_{1y}\,\bar{j} + S_{1z}\,\bar{k} - 2\,(N_{2x}\,\bar{i} + N_{2y}\,\bar{j} + N_{2z}\,\bar{k})\ \mathrm{DEL}$$

where

$$\mathrm{DEL} = S_{1x}N_{2x} + S_{1y}N_{2y} + S_{1z}N_{2z}$$

$$S_2 = (S_{1x} - 2N_{2x}\,\mathrm{DEL})\,\bar{i} + (S_{1y} - 2N_{2y}\,\mathrm{DEL})\,\bar{j} + (S_{1z} - 2N_{2z}\,\mathrm{DEL})\,\bar{k}$$

The direction cosines of the ray reflected from P (x_2, y_2, z_2) are now determined as

$$S_{2x} = S_{1x} - 2N_{2x}\,\mathrm{DEL}$$

$$S_{2y} = S_{1y} - 2N_{2y}\,\mathrm{DEL}$$

$$S_{2z} = S_{1z} - 2N_{2z}\,\mathrm{DEL}$$

Finally it is necessary to determine where this reflected ray intersects a plane perpendicular to the optical axis of the telescope. The linear transformation which was applied above has moved the location of the Gaussian focal plane to the X intercept $x = c$. Hence, the X coordinate of the intercept or "picture" plane is

$$x_F = c + m$$

where m is the amount this plane is displaced in the X direction from the Gaussian focus.

The magnitude of the vector connecting points P (x_2, y_2, z_2) and P (x_F, y_F, z_F) is denoted as T_2 and is illustrated in Figure 9. It then follows that

$$S_{2x} = \cos \alpha = \cos (180° + \theta) = - \cos \theta = - \left(\frac{x_2 - x_F}{2} \right)$$

$$x_F = x_2 + T_2 S_{2x} = c + m$$

Hence

$$T_2 = - \left(\frac{x_2 - c - m}{S_{2x}} \right)$$

and

$$S_{2y} = \cos \beta = \cos (90° + \theta) = - \cos \theta = - \left(\frac{y_2 - y_F}{T_2} \right)$$

$$y_F = y_2 + T_2 S_{2y}$$

$$S_{2z} = \cos \gamma = \cos (90° + \theta) = - \cos \theta = - \left(\frac{z_2 - z_F}{T_2} \right)$$

$$z_F = z_2 + T_2 S_{2z}$$

The true "picture" plane intercept P (x'_F, y'_F, z'_F) is finally determined by reversing the original angular transformation through ϕ. This is accomplished by the familiar equations

$$y'_F = y_F \cos \phi - z_F \sin \phi$$

$$z'_F = y_F \sin \phi + z_F \cos \phi$$

and

$$x'_F = c + m$$

ACKNOWLEDGMENT

I would like to acknowledge the valuable assistance of Mr. R. J. Porterfield II who implemented the above mathematical analysis into a useful computer program.

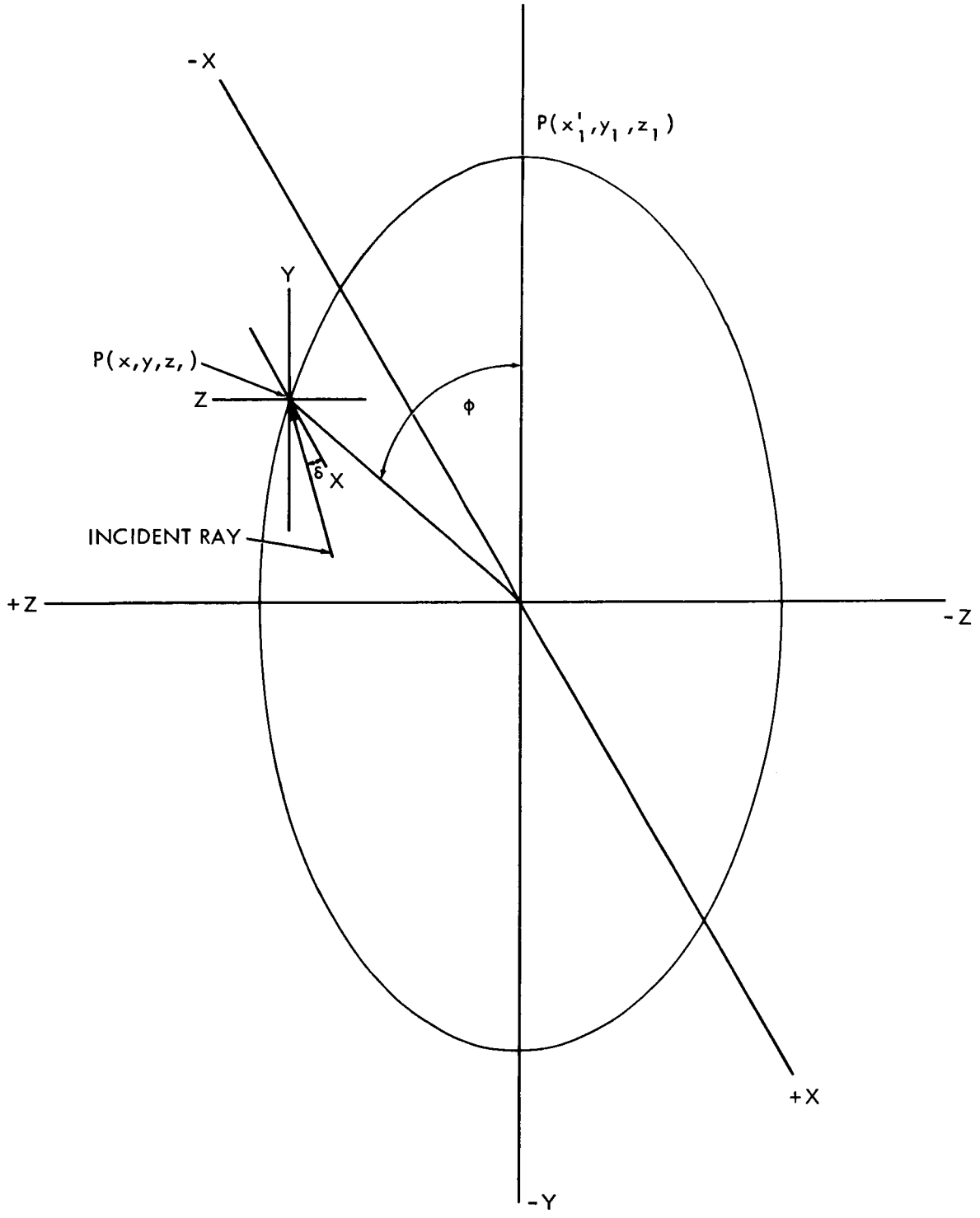

Figure 1

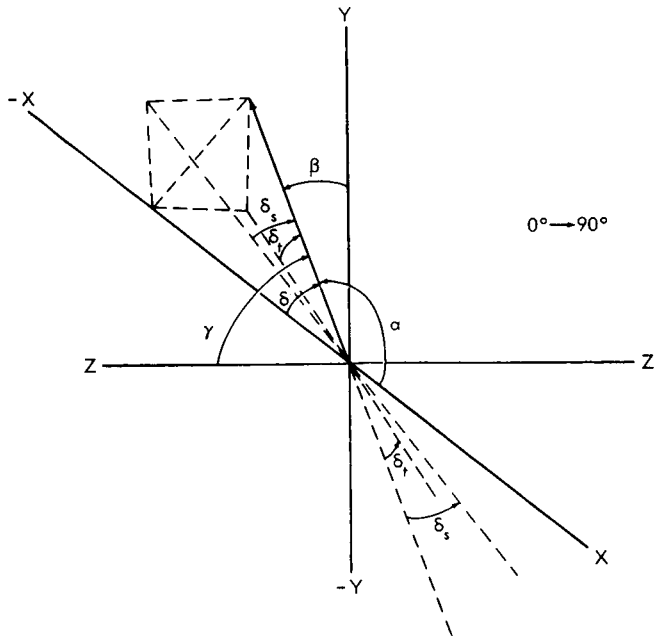

Figure 2

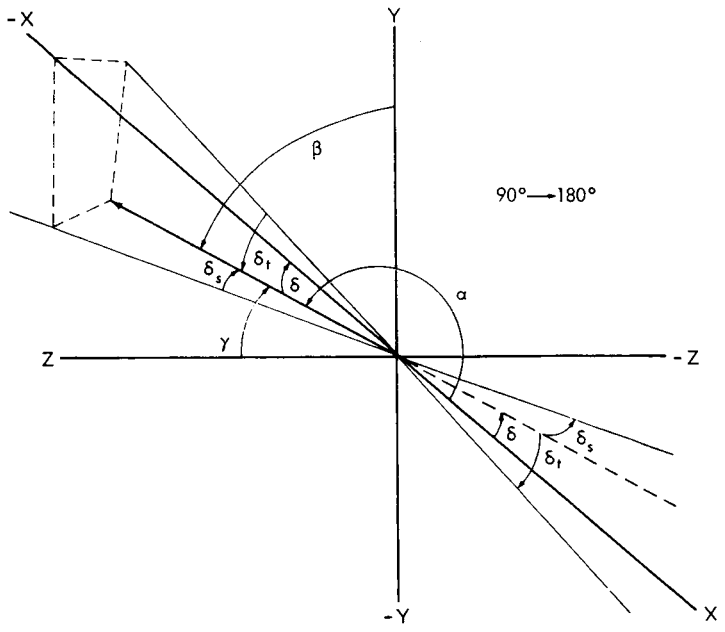

Figure 3

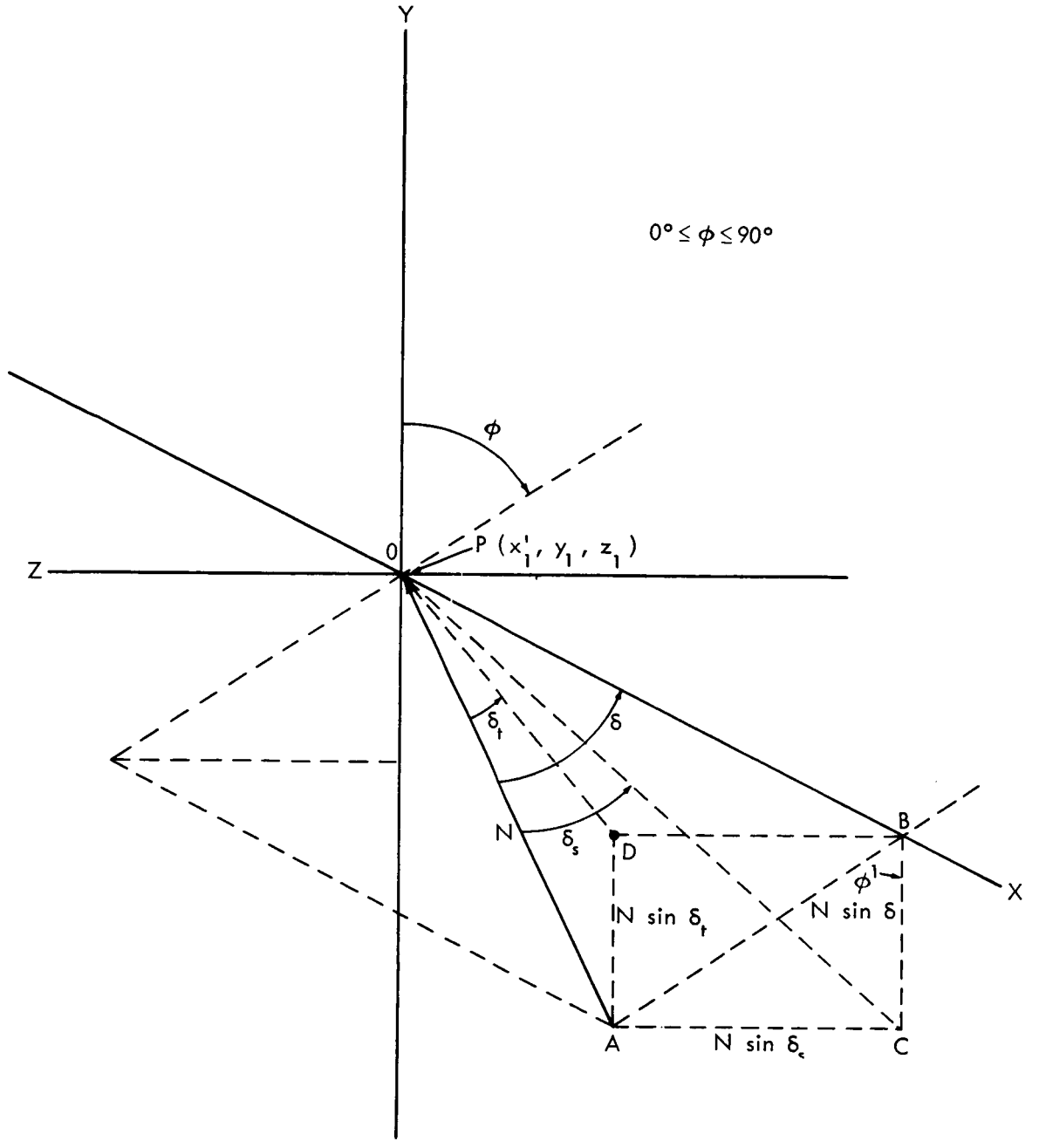
Y
$0° \leq \phi \leq 90°$
ϕ
Z
0
P (x_1', y_1, z_1)
δ_t
δ
N
δ_s
D
B
X
ϕ'
N sin δ_t
N sin δ
A
N sin δ_c
C

Figure 4

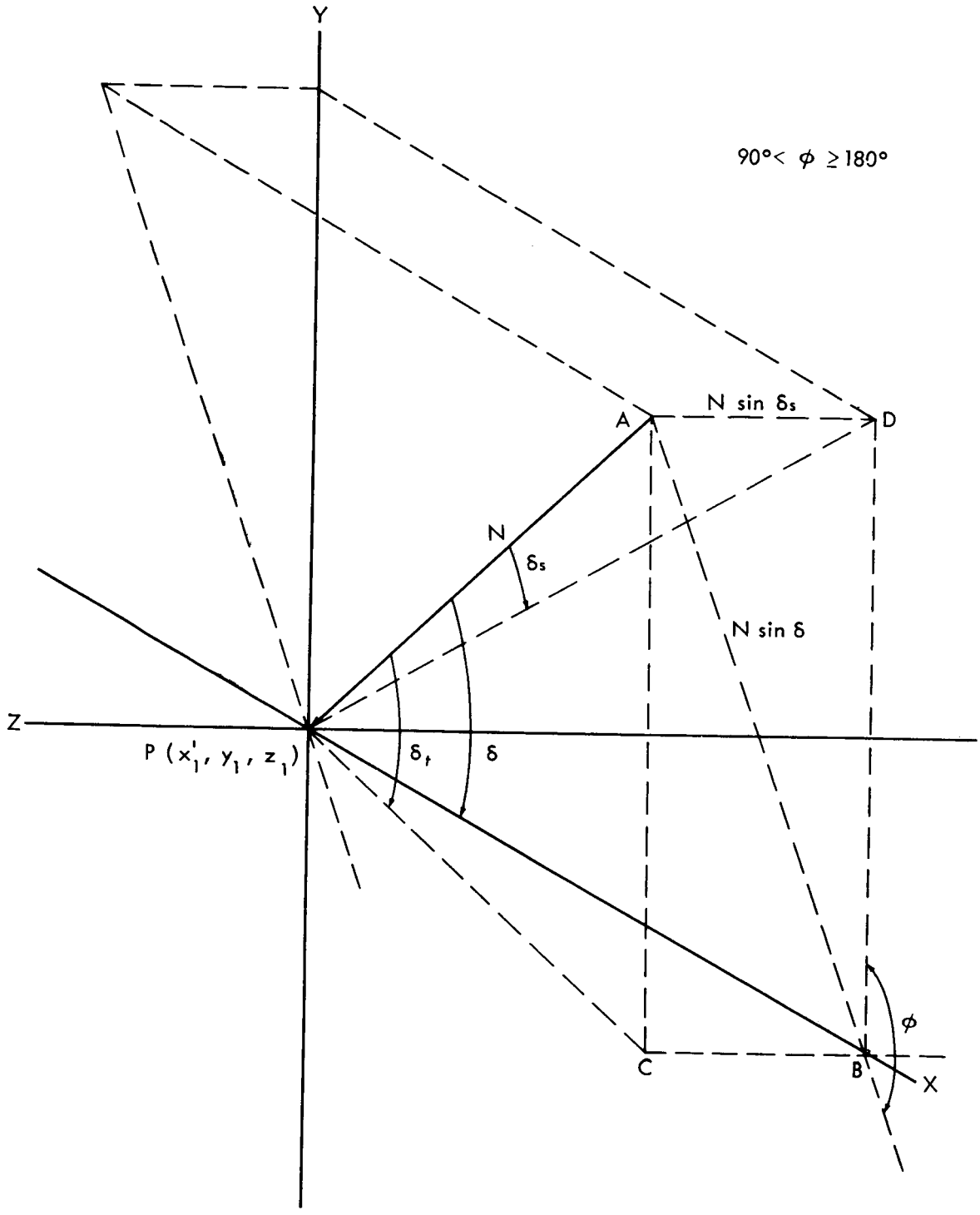

Figure 5

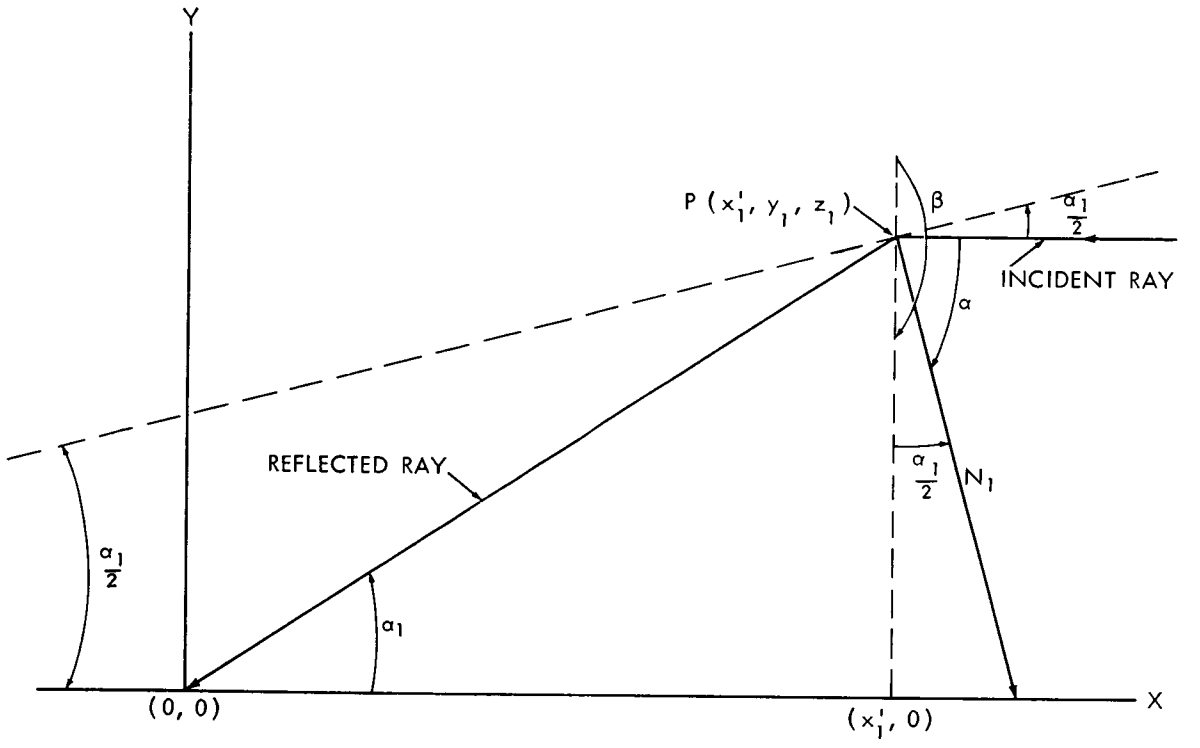
Y
P (x'1, y1, z1)
β
α1/2
INCIDENT RAY
α
REFLECTED RAY
α1/2
N1
α1/2
α1
(0, 0)
(x'1, 0)
X

Figure 6

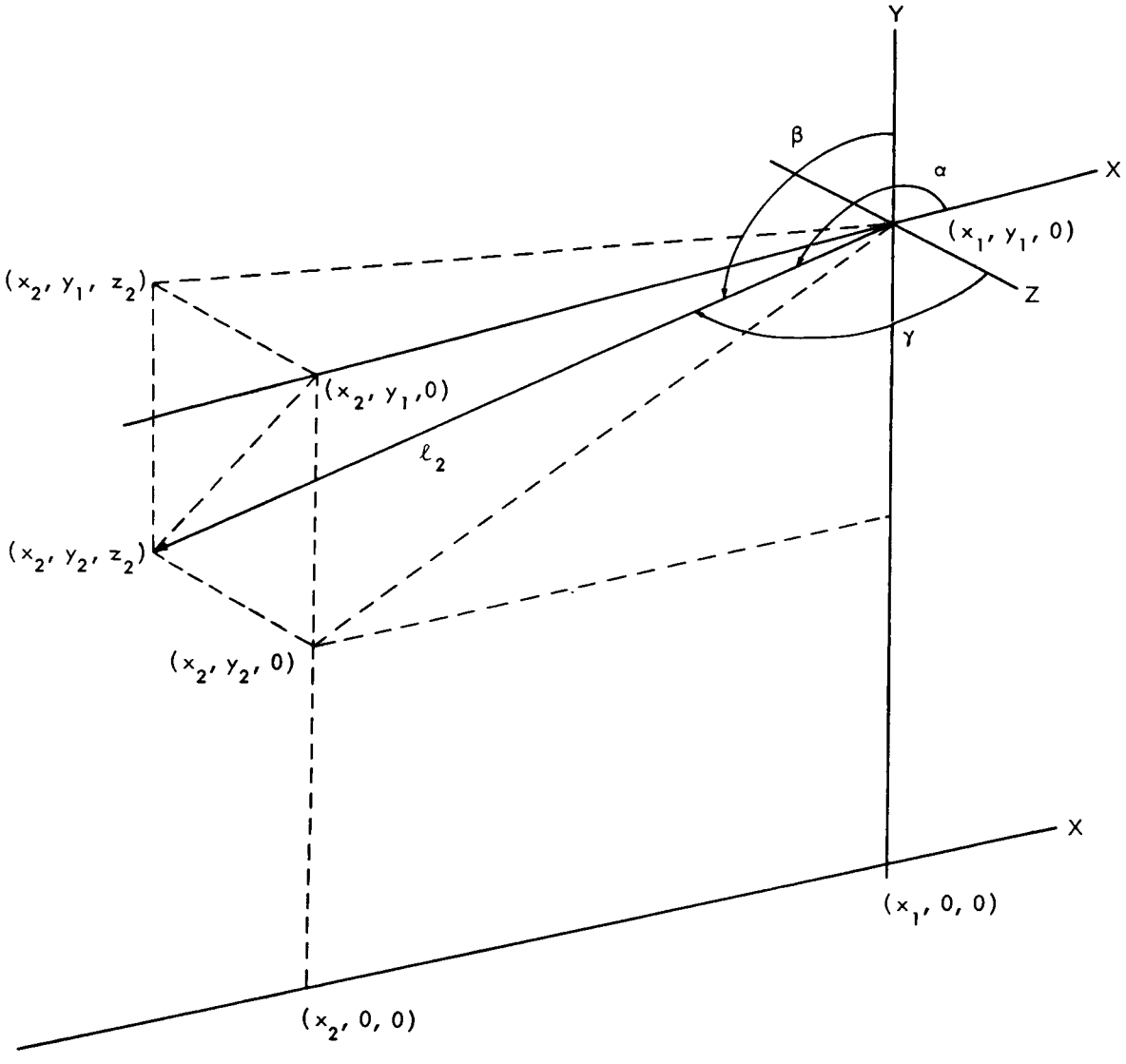

Figure 7

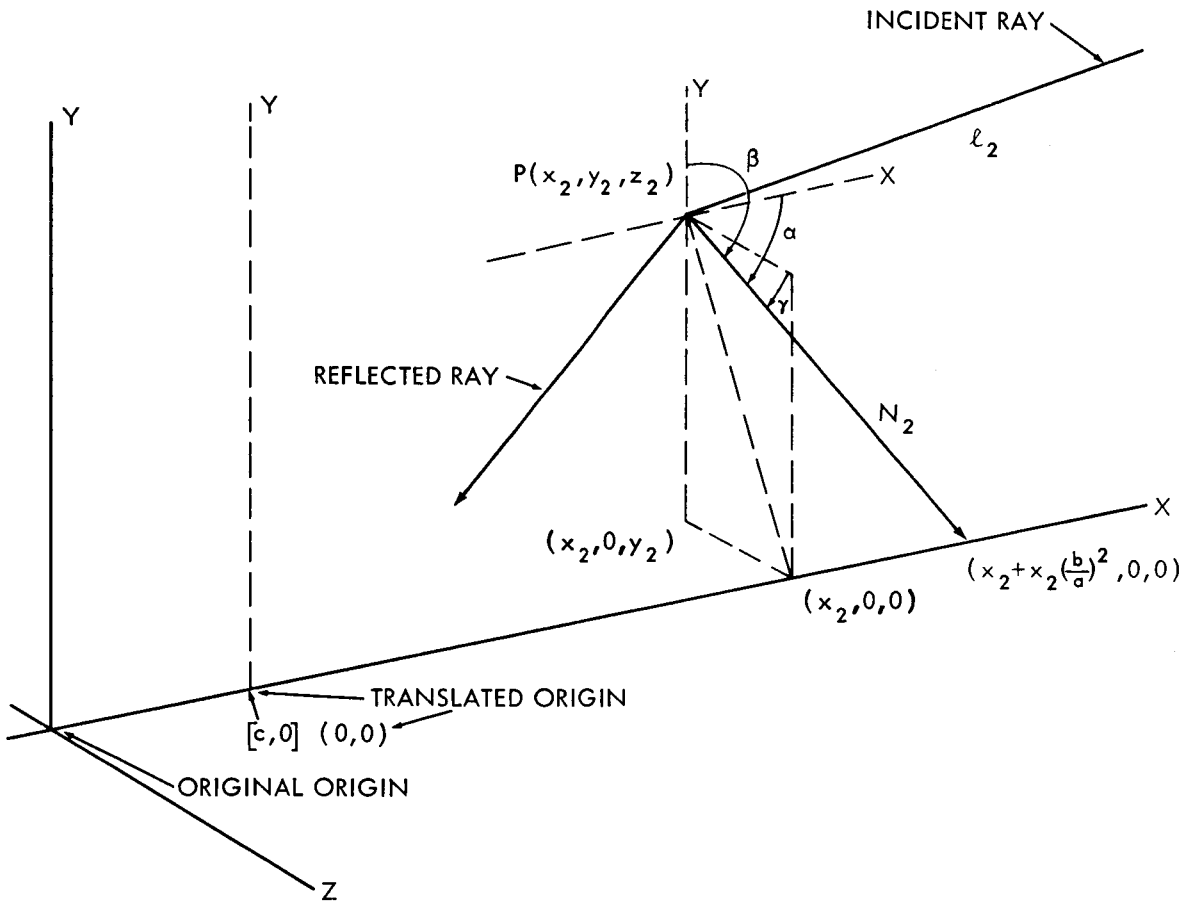
INCIDENT RAY
Y
Y
Y
$P(x_2, y_2, z_2)$
β
X
ℓ_2
α
γ
REFLECTED RAY
N_2
X
$(x_2, 0, y_2)$
$(x_2 + x_2(\frac{b}{a})^2, 0, 0)$
$(x_2, 0, 0)$
TRANSLATED ORIGIN
[c,0] (0,0)
ORIGINAL ORIGIN
Z

Figure 8

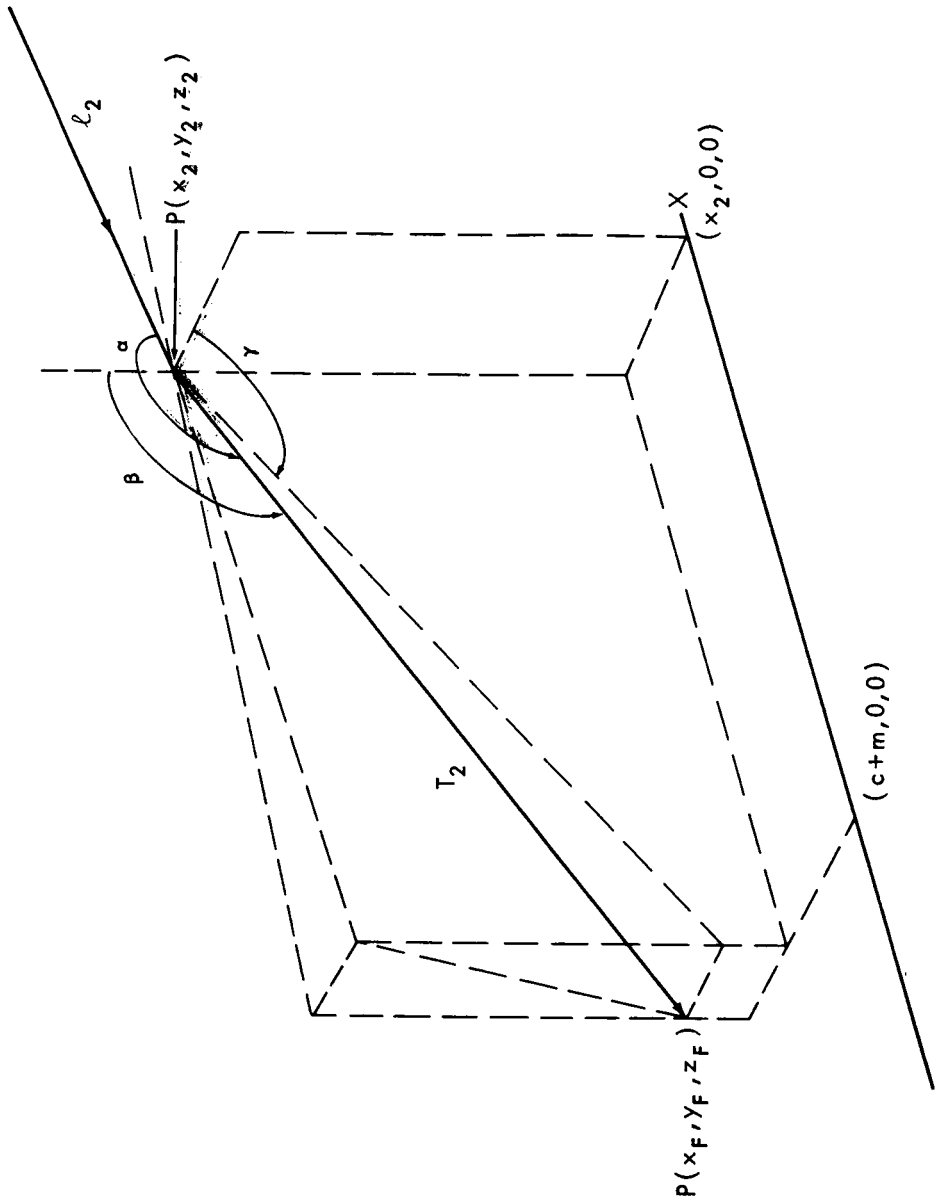

Figure 9